PHYSICAL REVIEW B **87**, 125117 (2013)

Nonlinear quenching of densely excited states in wide-gap solids

Joel Q. Grim,[1,*] K. B. Ucer,[1] A. Burger,[2] P. Bhattacharya,[2] E. Tupitsyn,[2] E. Rowe,[2] V. M. Buliga,[2] L. Trefilova,[3] A. Gektin,[3] G. A. Bizarri,[4] W. W. Moses,[4] and R. T. Williams[1,†]

[1]*Department of Physics, Wake Forest University, Winston-Salem, North Carolina 27109, USA*

[2]*Department of Physics, Fisk University, Nashville, Tennessee 37208, USA*

[3]*Institute for Scintillation Materials, Kharkov 1001, Ukraine*

[4]*Lawrence Berkeley National Laboratory, Berkeley, California 94720, USA*

(Received 21 January 2013; published 13 March 2013)

Dense interband electronic excitations on the order of 0.2 electron-hole pairs per nm^3 are encountered in a number of circumstances of fundamental and practical significance. We report measurements of the kinetic order and rate constants of nonlinear quenching in pure and doped materials with band gaps in the range from 6 eV down to 1.4 eV. The principal method used can be described as interband Z-scan luminescence yield with subpicosecond pulse excitations. A clear delineation of second-order and third-order quenching kinetics is found between oxide and iodide insulating crystals. This delineation suggests that the hot-electron thermalization rate mediated by LO phonon frequencies governs whether free carriers can pair as excitons within the time period of nonlinear quenching.

DOI: 10.1103/PhysRevB.87.125117 PACS number(s): 72.20.Ht, 78.70.Ps, 72.20.Jv, 78.55.−m

I. INTRODUCTION

High concentrations of excited states in solids can lead to rapid de-excitation with part of the energy converted ultimately to lattice vibrations. This has practical consequences in several systems of importance. The loss of excited states can be manifested as a loss of efficiency of light emission or LED droop[1–3] in laser diodes and solid-state illumination devices at high current density in a junction, quantum well, or quantum dot. The light emission from a densely excited particle track in scintillator radiation detectors suffers not only loss of total efficiency, but because the nonlinear quenching changes continually and stochastically along the track of a slowing particle, the energy resolution from counting photons is degraded by nonlinearity of light yield.[4–13] Energy-resolving radiation detectors are experiencing a resurgence of development activity for security monitoring of containers, medical molecular imaging, and experiments in high-energy physics and astronomy. In other areas such as laser damage in transparent materials, the nonlinear rate of conversion of electronic excitations to lattice temperature is also important. The amount and pathways of radiation damage in living tissue, especially approaching the track ends of ionizing particles, can similarly depend on the nonlinear quenching of excited states.

While the results and methods of this study can have general applicability in several of the fields listed above, the immediate context for the experiments reported here is the problem of understanding and quantitatively representing nonlinear light yield along the tracks of slowing electrons in scintillator radiation detectors. Thus the majority of materials chosen for this study are moderately wide-gap oxide and halide crystals. The same general phenomena governing nonlinear loss of electrons and holes to thermal energy as a function of local excitation density in a particle track can occur in semiconductor charge-collection radiation detectors as well as scintillators. CdTe and $Cd_{1-x}Zn_xTe$ (CZT) are therefore included in the present study. In numerical modeling studies of the interaction between nonlinear quenching and carrier diffusion,[9,10,14] we have found it useful to compare both insulators and semiconductors in order to include limiting cases of low and high mobility.

The experiments being reported are able to determine the kinetic order (second or third power of excitation density), the total quenched fraction as a function of excitation density, and the rate constant (K_2 or K_3) for dominant second- or third-order quenching. Measurement of total quenched fraction, when compared to track-end quenching from K-dip spectroscopy,[15] has allowed experimental determination of the track-end radius of the nonlinear quenching zone in a scintillator (NaI:Tl).

Nonlinear quenching rates in several wide gap materials useful for scintillator radiation detectors have previously been measured by time resolution of laser-excited luminescence decay time versus excitation density. Dipole-dipole quenching of closely spaced $(Ce^{3+})^*$ excited states in CeF_3 under both γ-ray and uv laser excitation was demonstrated by Nikl *et al.*[16] Kirm *et al.*,[17] Nagirnyi *et al.*,[18] and Laasner *et al.*[19] have studied the intrinsic excitonic scintillator $CdWO_4$, fitting decay time measurements versus excitation density to second-order quenching kinetics. We have conducted similar decay-time experiments on CsI excited in the exciton spectrum at or slightly below the band edge, finding second-order quenching kinetics in that case as well.[10,20] However, when exciting with higher photon energy relative to the band edge in CsI, the experiments reported in the present work find nearly pure third-order quenching. Nonlinear quenching remains nearly pure second-order in the measured oxide insulators that have band gaps less than our 6.1 eV laser photon energy, i.e., BGO ($Bi_4Ge_3O_{12}$) and $CdWO_4$. We shall suggest that the hot electron thermalization time is at the root of these distinctions. Electron thermalization is significantly slower in crystals with low optical phonon frequencies ω_{LO} such as the iodides, compared to oxides and fluorides with higher ω_{LO}.[21–25]

Time-resolved measurements have shown that in CsI:Tl and NaI:Tl, at least, the nonlinear quenching occurs mainly in the population of host excitations, not among the Tl^* excited activators.[10] Thus determination of nonlinear quenching rates by decay time analysis may be applicable only in materials

having reasonably bright luminescence of the host itself, whereas many scintillators depend on the activator ions for their bright emission. We designed the experiments, reported in this work, to measure the variation of total light yield with excitation density, rather than having to resolve the decay time of the specific quenching population.

This paper aims to experimentally determine the dominant kinetic order of nonlinear quenching across a number of iodide, oxide, and semiconductor materials that have band gaps accessible to the 6-eV laser photons used. It aims to compare the magnitude of nonlinear quenched fraction across most of that set of materials, corresponding to a given excitation density such as 10^{20} eh/cm^3. Furthermore, by fitting the light yield versus excitation density (Z-scan plot) with rate equation models, values of the nonlinear rate constants K_2 and K_3 are deduced. The set of materials chosen spans a considerable range of carrier mobilities, and effects of carrier diffusion interacting with nonlinear quenching can be observed.

II. EXPERIMENTAL METHOD

We use a method that may be summarized as interband Z-scan luminescence yield. Its similarity to Z-scan measurements as commonly employed to study optical nonlinearities in materials transparent to the laser beam[26,27] is that in both cases, a Gaussian laser beam profile including the beam waist is translated longitudinally through the sample while acquiring data. Both applications make use of the fact that the total power of the laser beam remains constant throughout the scan and that the predictable and measureable variation of the transverse profile of a Gaussian beam as a function of distance from the beam waist specifies the profile of optical energy density deposited in or passing through the sample. This makes for a clean measurement of nonlinearities in the sense that in absence of nonlinearities, the detected properties of transmitted (conventional Z scan) or absorbed and re-emitted (this work) optical signal should remain constant throughout the scan.

In the experiments reported here, the laser photon energy is above the fundamental absorption edge of the sample, so all incident energy after reflection is deposited and may then be re-emitted as luminescence unless quenched. The luminescence signal is measured as a function of the distance of the beam waist behind ($z < 0$) and in front ($z > 0$) of the sample surface. These are the data in raw form. Measurements of the transverse and longitudinal beam profile allow the conversion of z into a specific pulse fluence profile on the sample face. Knowledge of the optical absorption coefficient α at the excitation wavelength (and for the given laser fluence, in case of saturation)[10,19] then allows us to plot the light yield versus the on-axis excitation density n_0 in the volume element at the center of the laser spot and just under the entrance face of the sample.

The experimental setup is represented schematically in Fig. 1. The sample is placed in a polished aluminum enclosure (integrating sphere) and is oriented to reflect the ultraviolet laser beam back out through the entrance hole. Facing the sample at a 45° off-normal angle is a bialkali photomultiplier with a fused silica window. The 12-inch focal length S-1 grade silica lens is translated along the beam axis, thus moving the beam waist through the stationary sample surface, while the photomultiplier output is recorded with a boxcar averager.

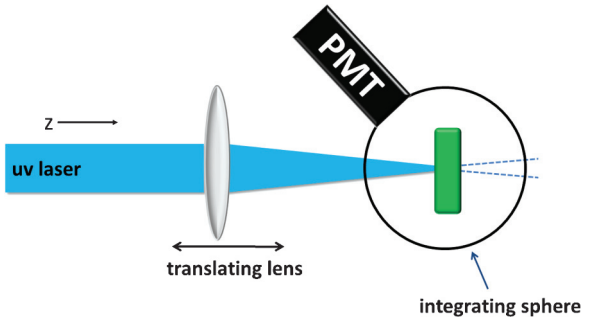

FIG. 1. (Color online) Illustration of the experimental setup used in interband Z-scan luminescence yield measurements of nonlinear quenching rates and kinetic order. A translating lens focuses a Gaussian beam that is absorbed by the sample. Luminescence photons are channeled into a photomultiplier.

The optical beam is the fourth harmonic of an amplified femtosecond Ti:sapphire laser. The repetition rate is 10 Hz and the duration of the amplified pulse is 0.5 ps. The fourth harmonic, generated in a BBO frequency doubler and redoubler combination, is tunable from 5.9 to 6.1 eV. Ultraviolet pulse energy is selectable in the range of 5–150 nJ with neutral density filters. The residual fundamental and second harmonic wavelengths are removed before the experiment chamber by filters and a pair of fused quartz dispersing prisms in the incident beam. The power of the fourth harmonic beam is measured with a Newport 818-UV photodetector with 883-UV filter. The beam profile is measured with a Thorlabs BC106-UV CCD profiler with an integrated M^2 analysis system. M^2 is a beam quality factor modifying the Gaussian beam radius $w(z)$ expressed as the following function of distance z from the plane of the beam waist:

$$w(z) = w_{0M}\sqrt{1 + \left(\frac{M^2\lambda z}{\pi w^2{}_{0M}}\right)^2}, \qquad (1)$$

where w_{0M} is the beam waist radius and λ is the wavelength.

The fourth harmonic from our system has a modified Gaussian beam characterized by $M^2 = 2.5$ for 5.9 eV light and $M^2 = 1.7$ for 6.1 eV light. A plot of the measured 5.9 eV fourth harmonic beam radius (points) as a function of position z and a fit to Eq. (1) with $M^2 = 2.5$ (line) is shown in Fig. 2. It illustrates that the Gaussian profile modified by the M^2 factor provides a good description even for the fourth harmonic of amplified pulses. Profile images of the 5.9 eV beam measured 3 cm from the beam waist and at the beam waist, respectively, are shown in Supplemental Material.[28]

From the on-axis laser fluence F_0, photon energy $h\nu$, and absorption coefficient α, the initial excitation density distribution is expressed as

$$n(r,z,\zeta,t=0) = \frac{F_0\alpha}{h\nu}e^{-2r^2/w^2(z)-\alpha\zeta} = n_0 e^{-2r^2/w^2(z)-\alpha\zeta}, \quad (2)$$

where r is the transverse radial coordinate on the sample surface, and z is the position along the beam axis relative to $z = 0$ at the beam waist. $w(z)$ is the $1/e^2$ radius of the irradiance profile on the sample surface for lens position

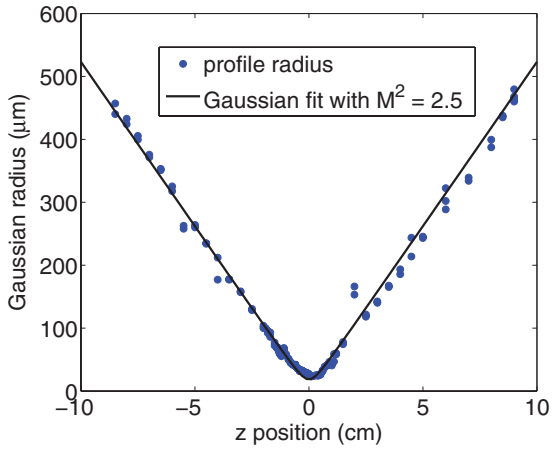

FIG. 2. (Color online) Measured fourth harmonic beam radius as a function of z position from the sample entrance surface to the beam waist for 5.9-eV light. The line is a fit to Eq. (1) with $M^2 = 2.5$.

z. The energy deposited is attenuated exponentially within the sample as $\exp(-\alpha\zeta)$, where α is the optical absorption coefficient and ζ is measured along the z axis with $\zeta = 0$ at the sample surface. The variable z is used here as a measure of lens translation, with $z = 0$ placing the beam waist at the sample surface.

Published values of the absorption coefficient α from reflectivity analysis or thin film transmission in the spectral range 5.9–6.1 eV exist for BGO, $CdWO_4$, NaI, ZnO, CdTe, and CZT (see Table I). We measured α in a CsI film using the 5.9 eV laser itself.[10] Reflectance at the laser wavelength of the sample and any cell windows is taken into account when relating incident fluence on-axis to the absorbed fluence F_0 used in Eq. (2). Z-scan data will be displayed versus lens position (z) on the lower horizontal axis. The upper horizontal axis will display the corresponding fluence at the center of the beam (in mJ/cm^2). When data for several materials measured at the same beam power and profile are displayed together, external fluence is labeled and reflectances for each material/cell are stated. When data for a single material are presented, both reflectance and absorption coefficient can be taken into account to display on-axis excitation density at the sample surface, n_0 (eh/cm^3), on the horizontal axis.

The sources and surface preparations were as follows: $Bi_4Ge_3O_{12}$ (St. Gobain) was polished to optical finish, and used in air; $CdWO_4$ (Kharkov) was cleaved and used in air; SrI_2 (Fisk) was polished with 0.05 μm alumina in mineral oil, finished in a dry box, and hermetically sealed in a sapphire window cell; CsI (Kharkov and Fisk) was polished with 0.05 μm alumina, and used in air; NaI (Kharkov) was dry polished in a glove box to avoid oil, and hermetically sealed in a quartz cell after heat treatment; NaI (St. Gobain) was given a commercial product polish and sealed in a quartz cell; CdTe and $Cd_{0.9}Zn_{0.1}Te$ (Fisk) were polished with 0.05 μm alumina, chemically etched with 5% Br_2/MeOH, and used in air; ZnO (Eagle Picher) was a single crystal epitaxial quality wafer, used in air.

It is important to rule out lattice heating and the associated thermal quenching of luminescence as a cause of the nonlinear quenching observed in these Z-scan experiments. There are three main arguments against lattice heating having a significant role in the conditions of this experiment, which are described in greater detail in Supplemental Material:[19,28–32] (1) we estimate the lattice temperature rise to be $\leqslant$37 K above room temperature even before taking into consideration the thermal diffusivity, (2) there is a sharp dependence of observed kinetic order on material class, and (3) we demonstrated that the shape of the Z-scan dip predicted for thermal quenching does not match the data. Laasner *et al.* estimated from a luminescence lifetime study of $ZnWO_4$ that femtosecond uv laser pulses strong enough to induce the substantial dipole-dipole quenching that they observed in $CdWO_4$ should produce $\leqslant$10 K in lattice temperature rise.[19]

III. ANALYSIS

The raw data measured in this experiment comprise light emission integrated over the nearly Gaussian radial profile, the exponentially attenuated longitudinal profile, and time. The time integral is over competing radiative and nonradiative rates, taking into account possible changes in identity or interaction characteristics of the excited population such as thermalization, pairing, or capture on activators. This is expressed as coupled rate equations for each distinct population. The diffusion of excitations to new spatial distributions during time integration can also be important especially in electron tracks as shown previously.[9,10,33,34] The electron track can be of order 3 nm (see Sec. IV G below), confining up to 2×10^{20} eh/cm^3, so the concentration gradient can be very large. The Z-scan laser experiment deposits energy in a slab of approximately 30-nm thickness depending on interband absorption coefficient. The one-dimensional gradient is about 10$\times$ lower than the two-dimensional radial gradient in electron tracks, so diffusion will not be explicitly included in the present analysis of Z-scan data on oxide and iodide insulators. But the higher carrier mobilities in the semiconductors CdTe and ZnO require inclusion of diffusion to fit the experimental Z-scan observations, as will be shown and developed in Sec. IV E.

A. Coupled rate equations for free carriers and excitons

The excitation by energetic particles such as fast electrons in scintillators produces several distinguishable but interacting populations whose evolution in time can be represented by coupled rate equations.[8] One can imagine at least four important populations including free carriers, excitons, trapped carriers, and trapped excitons, respectively. The practical problem is that the number of decay rates, including coupling rates between the populations, often outstrips the experimental information that is available as input for modeling such coupled systems accurately. Some simplifying assumptions are often needed, and this amounts to proposing hypothetical models for analyzing the integrated light yield data to extract rate constants. In the present case, we believe that the experimental observations reviewed briefly below provide justification for the hypotheses that simplify the set of coupled rate equations needed to analyze the data related to nonlinear quenching.

Several observations indicate that nonlinear quenching takes place fairly early in the evolution of excited states. In CsI, CsI:Tl, NaI, and NaI:Tl, nonlinear quenching occurs in the host populations of free carriers or excitons, rather than on dopant ions.[10] Transfer of electrons from the host excitons

to a Tl dopant has been observed by picosecond absorption spectroscopy to occur in a time of order 6 ps in CsI:Tl(0.3%),[35] implying that the observed nonlinear quenching in the host exciton population has occurred in the same time frame. At the end of the previous section, we noted that third-order quenching in iodides may imply that nonlinear quenching (NLQ) takes place within the hot electron thermalization time, ranging from 7 ps in CsI to 2 ps in NaI.[21,22] A streak camera measurement of the decay time of self-trapped exciton luminescence in CsI and NaI excited to densities of 2×10^{20} eh/cm^3 showed shortening of the decay time to the 20-ps range, limited by trigger jitter.[10] These observations suggest that nonlinear quenching may be adequately represented by coupled rate equations for only free carriers and excitons, with further coupling terms feeding some of the survivors into populations of trapped carriers and trapped excitons. The detrapping-retrapping and radiative processes leading to light yield from the latter populations generally occur on a slower time scale. We hypothesize that their associated rate equations have a significant role in scaling the total light yield, but do not directly contain nonlinear (density dependent) quenching rates of major significance.

Let n be the density of free electrons and holes in photoexcited or electron-excited intrinsic material (thus $n_e = n_h = n$). Let upper-case N be the density of excitons (bound state of an electron and hole). Although one may selectively create excitons in an experiment such as this one by tuning the laser to a bound state in the electron-hole spectrum, the excited states created initially by a high-energy electron, such as in scintillator applications, are predominantly free electrons and holes. For this purpose, we define free electrons and holes as those having kinetic energy in excess of the Coulomb energy binding one carrier to the nearest carrier of opposite sign. This would include thermalized carriers located beyond the Onsager radius[6,36] and hot carriers at closer distances to the nearest opposite carrier. Vasil'ev has plotted the calculated spectra of the imaginary part of the dielectric constant (ε_2) including exciton peaks, in comparison to a partial electron-hole contribution $\varepsilon_2^{\mathrm{eh}}$ excluding exciton peaks over the 10 eV–1000 keV range in BaF_2, for example.[37] The fraction of the total strength of transition into the bound-state exciton resonances over this energy range is very small, on the order of 1%. In the same study, Monte Carlo methods were used to simulate the fraction of electron-induced excitations going directly (on 0.4-fs time scale) into valence excitons. The fraction is about 1.5% in BaF_2.[37] Depending on the hot electron thermalization rate (e.g., <0.5 ps in oxides and fluorides, and up to 7 ps in CsI),[21,22] we assume that the initially free electrons and holes can lose energy to phonons and pair up as excitons on a picosecond or somewhat subpicosecond time scale.

The hypothesized rate equation for free carrier density n in a spatially uniform population (neglecting diffusion) is written as

$$\frac{dn}{dt} = -A_1 n - B_2 n^2 - K_3 n^3. \tag{3}$$

The generation term (not shown) is assumed to be instantaneous, producing the starting density $n(t = 0)$. The linear trapping rate of carriers on dopants and defects is represented by $A_1 n$, which will also be the coupling rate into the equation for evolution of trapped carriers. Although the trapping rate can be fast (on the similar picosecond scale at which we expect nonlinear quenching to compete), the reverse rate of ionization from deep traps [coupling population back into Eq. (3)], is considered to be slower and is thus neglected in the present treatment. We do not explicitly represent separate trapping rates for electrons and holes, which would necessitate separate rate equations for n_e and n_h. This is a simplifying approximation that we believe is adequate for the present intent of illustrating main features of analysis at high carrier densities in excited insulators where $n_e \approx n_h$. The approximation $n_e \approx n_h \approx n$ is often made in treatments of third-order quenching and second-order radiative decay in intrinsic semiconductors.[38–40]

The bimolecular rate $B_2 n^2$ represents pairing of electrons and holes to form excitons, and thus is identical to the coupling rate into the exciton population N. The population N decays according to Eq. (4) below, including the production of light. For reasons similar to those given above for deep traps, we include the forward transfer rate $B_2 n^2$ from free carriers to excitons as a fast process competing with nonlinear quenching, but we neglect the reverse transfer from excitons (including self-trapped excitons) back into the free carrier equation by thermal ionization, as a slower process than the relevant 10-ps time scale. Finally, the rate $K_3 n^3$ in Eq. (3) represents free-carrier Auger recombination. This process eliminates one electron and one hole from the population represented by n, and so is not a coupling term into any other rate equation. Third-order quenching to the ground state by free-carrier Auger recombination is represented directly by the last term in Eq. (3). Whether the remainder of carriers coupled out through the first two terms ultimately emit light or are quenched in other kinetic orders depends on the solution of the rate equations fed by those two terms, respectively.

We now consider the rate equation for excitons at density N:

$$\frac{dN}{dt} = B_2 n^2 - C_1 N - K_2 N^2. \tag{4}$$

The source term $B_2 n^2$ represents the population transfer from the free-carrier Eq. (3), where we have made the model approximation that all excitations are initially free carriers based on the discussion two paragraphs earlier. The linear rate $-C_1 N$ is a sum of rates for first-order radiative decay of excitons (rate constant R_1), linear quenching to the ground state (rate constant Q_1), and trapping or scavenging of the exciton on a dopant ion or defect as stored energy (storage rate constant S_{1e}), which is the coupling term into the population of trapped excitons. Delayed light may ultimately be produced from the trapped carrier population with probability ρ. Exciton-exciton interaction leading to quenching is represented by the bimolecular rate $-K_2 N^2$. Dipole-dipole annihilation is a case of Förster transfer to another excited dipole rather than a ground-state dipole. The dipole-dipole transfer rate w_{dd} depends on the separation distance r_{sep} as

$$w_{dd}(r_{\mathrm{sep}}) = \tau_R^{-1} \left(\frac{R_{dd}}{r_{\mathrm{sep}}} \right)^6, \tag{5}$$

where τ_R is the radiative lifetime of the excited state and R_{dd} is the Förster transfer radius.[17,41] The second-order rate

parameter K_2 appearing in Eq. (4) is expressed in these terms for *immobile* species[17,41] as

$$K_2(t) = \tfrac{2}{3}\pi^{3/2} R_{dd}^3 (t\tau_r)^{-1/2} = \kappa_2 t^{-1/2}. \quad (6)$$

This time-dependent rate parameter $K_2(t)$ should be used at the place of K_2 in Eq. (4) when the interacting species are (nearly) immobile self-trapped excitons, which is the case in all iodides and oxides studied in the present work. The time dependence of $K_2(t)$ comes from the known result in bimolecular theory[10,17,41–43] that when decaying species are immobile, an initially uniform spatial distribution does not remain uniform as decay proceeds. The average pair separation departs from simply $N^{-1/3}$ because the closest pairs decay first, hollowing out an expanding void in a plot of pair number versus pair separation. In contrast, the distribution of mobile free carriers remains spatially uniform as decay proceeds, so K_3 in Eq. (4) is a simple constant when analyzing free carriers. The right-hand term of Eq. (6) identifies the constant portion of the expression for $K_2(t)$ as $\kappa_2 = 2/3\pi^{3/2} R_{dd}^3 \tau_R^{-1/2}$. The constant κ_2 will be reported throughout the remainder of this paper as the second-order rate constant, with an understanding that $K_2(t)$ specified in Eq. (6) is the actual rate parameter multiplying N^2 in Eq. (4) and subsequent expressions based on it. Except for exciton-exciton collision luminescence (the so-called P band) encountered in some semiconductors such as ZnO,[44] we do not know of another second-order exciton radiative process, and so neglect that possibility in writing Eq. (4).

The cases in which we have experimentally found second-order quenching are oxides in which carrier thermalization is sub-pico-second (with pairing to excitons presumed to follow), and NaI:Tl, CsI:Tl photoexcited in the exciton spectrum at 5.9 eV (see Sec. IV D below). We neglect the source term $B_2 n^2$ in favor of specifying a starting exciton density $N(t = 0)$ and write

$$\frac{dN}{dt} = -(R_1 + Q_1 + S_{1e})N - K_2(t)N^2 \quad (7)$$

as the rate equation to be solved for oxides and other cases of second-order quenching. In an intrinsic excitonic scintillator such as the undoped oxides $CdWO_4$ and BGO and undoped CsI, there is not a significant dopant trapping rate (S_{1e}) operating, so the linear rate constant is just $R_1 + Q_1$. The resulting rate equation is the same as already used in published excitation-dependent decay-time analyses of $CdWO_4$[17–19] and undoped CsI excited in the exciton bands.[10] For example, in undoped CsI, we found that the family of self-trapped exciton luminescence decay curves as functions of excitation density could be fit with $(R_1 + Q_1) = \tau_{obs}^{-1} = (1.4\ \text{ns})^{-1}$ and $K_2(t) = 2.4 \times 10^{-15}\ \text{cm}^3\text{s}^{-1/2}\text{t}^{-1/2}$. Since Nishimura *et al.*[45] had independently determined $R_1 = (15\ \text{ns})^{-1}$, we could deduce $Q_1 = (1.5\ \text{ns})^{-1}$, attributed to surface quenching when ultraviolet excitation is used.[10]

The Z-scan results on alkali and alkaline earth iodides to be presented in Secs. IV C–IV E below exhibit nearly pure third-order quenching, and so will be analyzed in terms of free-carrier rates up to the third-order given in Eq. (3). The data and discussion of Secs. IV B–IV F raise the interesting question of why excitations interact as free carriers in one class of materials and as excitons in another. Semiconductors at room temperature can often be well described in terms of free carriers simply because the exciton binding energy is smaller than or comparable to kT. But the oxide and halide insulators that are the main focus of this study have exciton binding energies on the order of 0.3 eV. What else could lead to carriers remaining free in the iodides and pairing to excitons in oxides during the time of main nonlinear quenching? A hypothesis to be developed in this paper is that the electron thermalization time compared to the nonlinear quenching time is responsible. The hot electron thermalization time for electron energies of a few eV has been calculated as 7 ps in CsI and 2 ps in NaI, compared to 0.5 ps in CaF_2 and $\leqslant$0.5 ps in complex oxides.[21,22]

To incorporate this extra time dependence of carrier thermalization as a hypothesis in the rate equations used for fitting, we assert that the coupling rates into exciton formation ($B_2 n^2$) and carrier trapping ($A_1 n$) cannot turn on until it becomes possible to trap electrons on holes or on dopants, i.e., until the electron has thermalized to within the trapping potential depth. Since we are not yet able to deal with the details of capture rates into individual trapping levels, we will assert as an approximate model that the trapping and bimolecular exciton formation channels turn on after a hot electron thermalization time that is approximated as 6 ps in iodides. The free-carrier Auger recombination is similarly modeled as turning off when the carriers thermalize and trap. In studies of Auger rates, particularly in insulators, high temperature raises the rate of Auger recombination significantly by expanding the range of k space in which momentum and energy can be conserved in the final states.[2,38] In addition, the self-trapping of holes in iodides together with the extended range of hot electrons imply that when electron thermalization and trapping finally occur, many of the electrons and holes will be spatially separated and not subject to Auger decay. Putting these hot-carrier model assumptions explicitly into Eq. (3), we write

$$\frac{dn}{dt} = -A_1 n\Theta(t - 6\ \text{ps}) - B_2 n^2 \Theta(t - 6\ \text{ps}) - K_3 n^3 \Theta(6\ \text{ps} - t), \quad (8)$$

where $\Theta(t - 6\ \text{ps})$ is the Heaviside step function turning on after 6 ps, and $\Theta(6\ \text{ps} - t)$ turns off after 6 ps.

This model is admittedly simplistic on the time dependence and can later be made to include more quantitative treatment of carrier thermalization and trapping, but it seems sufficient to make simple tests of how thermalization-dependent (thus time-dependent) rate constants that switch on or off more slowly in iodides than in oxides can lead to the striking difference of observed kinetic order of quenching in two different material classes. Without the stepped turn-on of the second-order term only after thermalization in Eq. (7), mixed second- and third-order kinetics would be observed, in contradiction to the experiments on iodides reported in this work. The rate constant K_3 appearing in Eq. (7) can be extracted after performing the integrations of the rate equations over time and space as described below, and fitting the data.

B. Integrating over r, ζ, and t

Assuming that every absorbed photon in the low interband spectrum results in the creation of one electron-hole pair, the initial carrier density distribution has the form shown in Eq. (2).

This serves as the initial density distribution for the integration of the nonlinear differential equations given in Eqs. (7) and (8) to find $N(\vec{r},t)$ of excitons or $n(\vec{r},t)$ of free carriers, respectively.

1. Excitons

The solution of Eq. (7), describing decay of a population of immobile excitons specified in cylindrical coordinates appropriate to the Z-scan method, can be written as

$$N(r,\zeta,z,t) = N_0(r,\zeta,z,0)e^{-t/\tau} \times [1 + N_0(r,\zeta,z,0)K_2\sqrt{\pi\tau}\,\mathrm{erf}(\sqrt{t/\tau})]^{-1}, \quad (9)$$

where $\tau = (R_1 + Q_1)^{-1}$for undoped excitonic scintillators with $S_{1e} = 0$. The initial excitation profile $N_0(r,\zeta,z,0)$ was given in Sec. II as Eq. (2).

For second-order quenching of self-trapped exciton populations, the integrated light yield LY_{exc} as a function of lens position z can then be written as

$$LY_{\mathrm{exc}}(z) = \frac{\int_0^\infty R_1 N(r,\zeta,z,t)d^2\vec{r}\,d\zeta\,dt}{\int_0^\infty (R_1 + Q_1)N(\vec{r},t) + K_2N^2(\vec{r},t)d^3\vec{r}\,dt} = \frac{1}{\eta_{\mathrm{tot}}}\int_0^\infty R_1 N(\vec{r},t)d^3\vec{r}\,dt, \quad (10)$$

where η_{tot} is the total number of excited states produced in the volume of integration, not to be confused with the population densities n and N. The full integration variables are shown only in the first numerator term on the right side and elsewhere represented by $N(r,t)d^3r$. When analyzing second-order quenching in insulators, we have assigned $(R_1 + Q_1) = 1/\tau_{\mathrm{eff}}$, where τ_{eff} is the measured decay time at room temperature for near-surface ultraviolet excitation appropriate to this experiment. The effective lifetime τ_{eff} for near-surface excitations even in some insulators includes diffusion to surface quenchers in addition to the true first-order bulk decay rates given here as R_1 and Q_1.[10,31] This is our approximation for the practical use of Eq. (10) to analyze insulators with modest diffusion. To analyze semiconductor Z scans in Sec. IV E, we will explicitly solve the diffusion along with the kinetic rate terms.

In Tl-doped CsI, scavenging of electrons from host excitons by the Tl dopant has been observed with picosecond absorption spectroscopy.[35] Using $S_{1e}N$ to represent the rate of such scavenging of excitons with a possibility of later radiative emission from a fraction ρ of the trapped carriers upon hopping recombination, the light yield in such a doped scintillator can be represented as

$$LY_{\mathrm{doped}}(z) = \frac{\int_0^\infty (R_1 + \rho S_{1e})N(\vec{r},t)d^3\vec{r}\,dt}{\int_0^\infty (R_1 + Q_1 + S_{1e})N(\vec{r},t) + K_2N^2(\vec{r},t)d^3\vec{r}\,dt}. \quad (11)$$

If the scavenging or storage rate S_{1e} is fast, such as $(6\ \mathrm{ps})^{-1}$ observed in CsI:Tl(0.3%),[35] the effect is to terminate the host exciton population quickly in competition with second-order quenching, without sacrificing ultimate light yield if the recovery fraction ρ is large.

To connect with the quantities previously introduced in the numerical modeling in Refs. 9, 10, 33, and 34, we note that the second-order quenched fraction QF_2 can be expressed in the present terms as

$$QF_2 = \frac{1}{\eta_{\mathrm{tot}}}\int_0^\infty K_2(t)N^2(\vec{r},t)d^3\vec{r}\,dt, \quad (12)$$

where $N(\vec{r},t)$ was modeled as dependent on the diffusion in electron tracks.

The linear quenched fraction k_1, which was also used in the numerical modeling of Refs. 9, 10, 33, and 34, is defined as

$$k_1 = \frac{1}{\eta_{\mathrm{tot}}}\int_0^\infty Q_1 N(r,t)d^3\vec{r}\,dt. \quad (13)$$

2. Free carriers

We solve Eq. (8) for third-order quenching in a decaying population of free carriers subject to the thermalization consequences modeled by the step functions to find $n(r,\zeta,z,t)$, where $n_0(r,\zeta,z,0)$ was specified for the Z-scan method by Eq. (2). That is, we hypothesized in writing Eq. (8) that the carriers remain free and experience free-carrier Auger quenching as long as they are hot. Upon thermalization, the survivors of Auger quenching can form excitons or trap on dopants and subsequently emit light. Thus, during the crucial time of third-order quenching of hot (free) carriers, Eq. (8) has only the third-order term active. Light yield through the second- and first-order terms will come more slowly from the surviving population. Therefore curve fitting of the Z-scan light yield data involves calculating the third-order quenched fraction QF_3:

$$QF_3 = \frac{1}{\eta_{\mathrm{tot}}}\int_0^{\tau_{\mathrm{therm}}} K_3 n^3(\vec{r},t)\,d^3\vec{r}\,dt. \quad (14)$$

IV. RESULTS AND DISCUSSION

A. Paradigms of interband Z-scan signatures

Figure 3 shows the four main paradigms of above-gap Z scans that we have observed in insulators and semiconductors, plotting normalized light yield versus position of the beam waist relative to the entrance face of the sample. Light yield is normalized to the left wing when net quenching is observed at $z = 0$, and to the peak when net enhancement of light yield is observed at $z = 0$. The behavior illustrated by SrI_2 in Fig. 3(a) has been found characteristic of alkali or alkaline earth iodide crystals measured so far when excited above the interband edge. The dip is narrow and can be well fitted by the third-order rate equation. It is not possible to force a second-order fit on the Z scans in such cases.

The behavior illustrated by BGO ($Bi_4Ge_3O_{12}$) in Fig. 3(b) has been found to be a characteristic of both oxide insulators measured so far. The dip is wider than in Fig. 3(a) and can be fit by the second-order rate equation, to the exclusion of third-order kinetics.

The Z scans of light yield from semiconductors with high carrier mobilities such as CdTe and CZT are inverted relative to the insulator Z scans, exhibiting a peak rather than a dip for the beam waist at the sample surface. The high carrier mobilities play two roles in producing such a peak. First, high mobilities allow some carriers to escape the thin

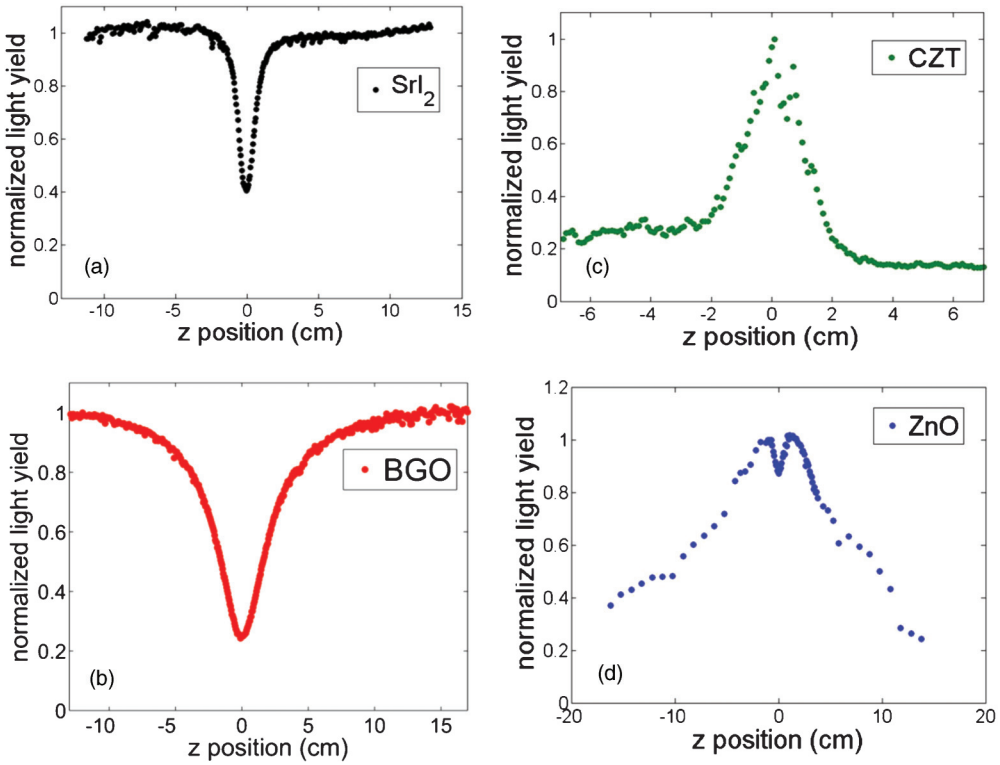

FIG. 3. (Color online) Z scans exhibiting (a) third-order Auger recombination in SrI_2. (b) second-order dipole-dipole quenching in BGO. (c) Bimolecular radiative recombination in CZT competing with quenching on saturable surface sites. (d) ZnO with intermediate carrier mobilities exhibits both nonlinear quenching dip and sloping wings.

(∼30 nm) ultraviolet excitation layer before significant nonlinear quenching at the highest densities can occur. A similar phenomenon for cylindrical electron tracks was demonstrated in the numerical modeling of Ge versus CsI.[10,14] Second, the exciton binding energy is small in most semiconductors, so that the dominant radiative rate at room temperature is bimolecular electron-hole recombination, which is enhanced by higher carrier density. Diffusion to the surface provides a competitive linear quenching rate that may saturate to a constant quench rate at high carrier density. A bimolecular radiative rate competing with linear or constant quenching rates leads in general to a rise of light yield versus excitation density.[8]

ZnO is a wide-gap semiconductor with more modest carrier mobilities ($\mu_e = 105$ cm^2/Vs, $\mu_h = 35$ cm^2/Vs)[46] than in CZT ($\mu_e = 1100$ cm^2/Vs, $\mu_h = 100$ cm^2/Vs).[47] The form of the Z scan in Fig. 3(d) suggests that carriers cannot escape the excitation layer fast enough to entirely avoid nonlinear quenching, hence the dip persisting near the beam waist.

B. Kinetic order and rate constants of nonlinear quenching in BGO and $CdWO_4$

Figures 4 and 5 show the data for BGO and $CdWO_4$, respectively, along with the best fits to second-order (solid) and third-order (dashed) quenching models described in Sec. III. The second-order theory expressed in Eqs. (7) and (9)–(11) is seen to fit BGO very well, but there is no value of K_3 that can force the third-order theory expressed in Eqs. (3), (8), and (14) into an agreement with the BGO data. Likewise, $CdWO_4$ is well fit by second-order quenching kinetics, while third-order theory predicts a central dip that is clearly too narrow.

The fit in Fig. 5(b) is not as good as the others because of an asymmetric elevation of the right wing ($z > 0$) attributed to an uncontrolled artifact of the experimental system. An asymmetry between left and right wings must involve something other than the z-dependent variation of fluence on the sample, which should be symmetric in z. Conventional Z-scan experiments in transparent samples show asymmetries associated with nonlinear effects on the transmitted beam,[27] but in our experiment, the beam is fully absorbed in about 100 nm. An asymmetry could be produced if there were progressive laser damage of the surface as the Z scan proceeds. To check this, we acquired data scanning in both directions, and the asymmetry was independent of scan direction. The asymmetry will be seen in varying degrees for several samples throughout this paper. In general, it is found to be more serious when the detected light level is low intrinsically or because of sample cell or surface quality issues bearing on light collection. This implies that the problem may originate from a weak background light signal that depends on lens position. We have tested for possible sources of background depending on the lens position z. One source, peculiar to uv excitation and therefore difficult to isolate or eliminate, is the fluorescence of the interior of the light-capture chamber when struck by scattered uv light that fails to be specularly reflected back out the beam entrance. For this reason, we avoided a conventional white-painted or ceramic integrating sphere, and chose an aluminum chamber to minimize fluorescence.

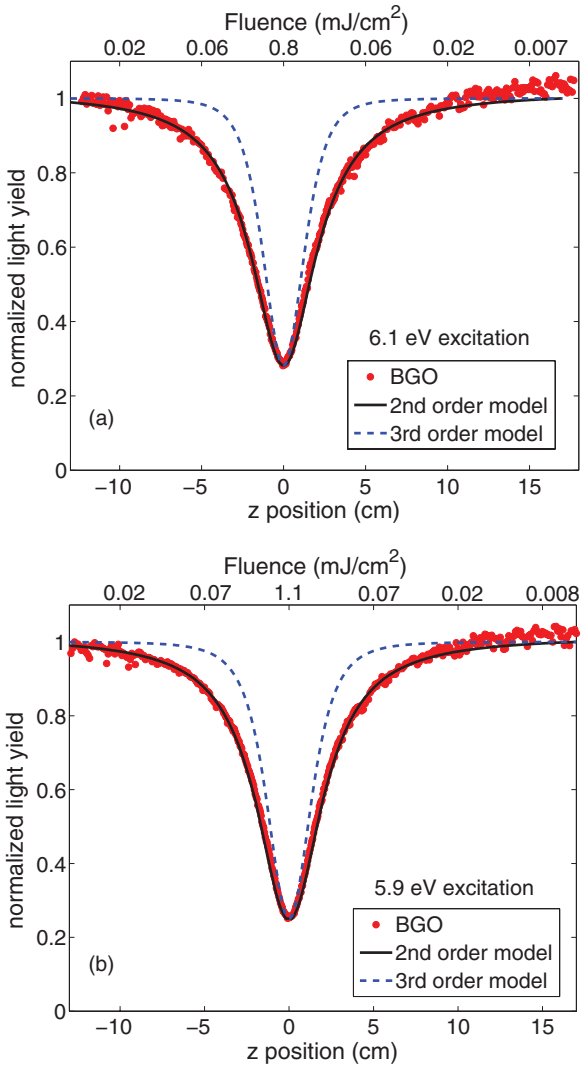

FIG. 4. (Color online) BGO Z-scan data (points) for (a) 6.1-eV and (b) 5.9-eV laser photon energy. The data can be fit by second-order quenching Eqs. (7) and (9)–(11) with $\kappa_2 = 1 \times 10^{-17}$ cm^{3}s$^{-1/2}$ (solid line). The best attempt to fit with third-order kinetics using Eqs. (3), (8), and (14) (see dashed line) is also shown. The light yield is normalized to its maximum value, which occurs in the wings for large $|z|$ where the excitation density is lowest.

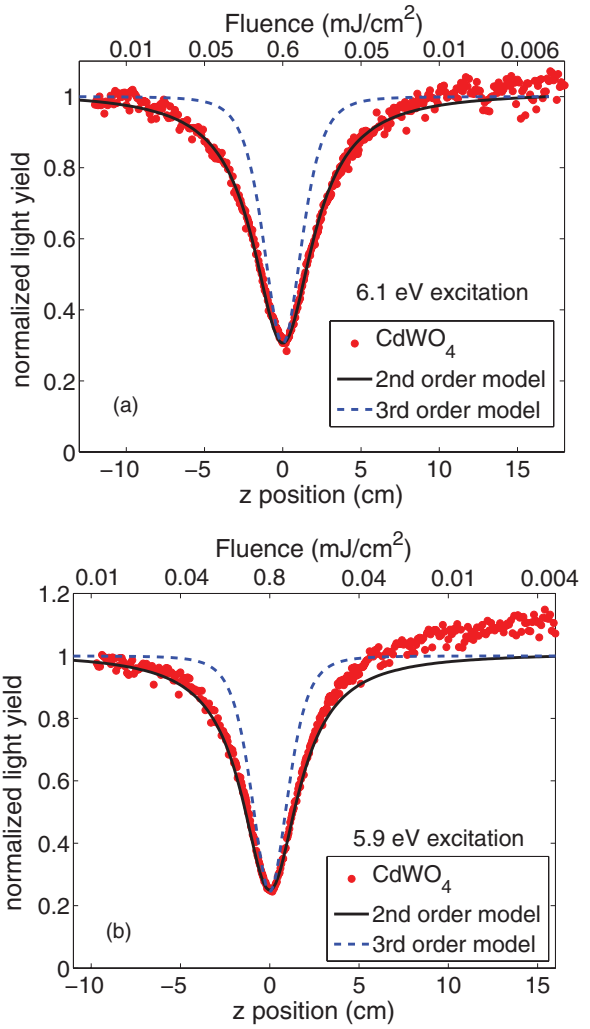

FIG. 5. (Color online) $CdWO_4$ Z-scan data (points) measured with (a) 6.1-eV and (b) 5.9-eV laser photon energy. The data are fit by second-order quenching with (a) $\kappa_2 = 3 \times 10^{-18}$ cm^{3}s$^{-1/2}$ and (b) $\kappa_2 = 2.9 \times 10^{-18}$ cm^{3}s$^{-1/2}$ (solid line). The attempt to fit with third-order kinetics (dashed line) is also shown

In the end, a small residual asymmetry remains for some samples depending possibly on different uv scattering pattern or collection path. We have chosen to normalize data consistently at the left wing, so the left side of the Z scans becomes the best place to look at comparisons of different samples.

The reported band gaps of BGO and $CdWO_4$, respectively, are 4.3 eV (see Ref. 48) and 4.75 eV $\pm$ 0.25 eV (the latter an average of two separate measurements).[49,50] Thus free carriers with an excess kinetic energy per pair of about 1.7 eV in BGO and 1.3 eV in $CdWO_4$ are produced initially in our experiments using 5.9 to 6.1 eV photon energy. Figures 4 and 5 together with their second-order fits imply that the free carriers have paired to form interacting dipoles before the majority of nonlinear quenching takes place.

C. Kinetic order and rate constants of nonlinear quenching in SrI_2

SrI_2 presents a clear case of third-order quenching as can be seen from the red solid line fit to the third-order model in Fig. 6. The best attempt at a second-order fit with the broken blue line is quite far from the data. Due to its free-carrier band gap of about 5.5 eV at room temperature,[51,52] SrI_2 was the first of the iodide crystals that we measured for which the 5.9 eV photon energy is definitely above the free-carrier interband edge. The third-order fit implies that the excitations are independent electrons and holes undergoing free-carrier Auger decay throughout the duration of nonlinear quenching. In intrinsic crystals, the density of absorbed photons, $n_{\rm ph}$, is equal to the initial densities of free electrons and free holes, $n_{\rm ph} = n_{e0} = n_{h0}$. Therefore free-carrier Auger rates proportional to $n_e n_e n_h$ and $n_e n_h n_h$ are proportional to the cube of the initial excitation density, $n_{\rm ph}^3$.[38,40]

We can directly see the distinction between kinetic orders of nonlinear quenching in SrI_2 versus BGO by a simple

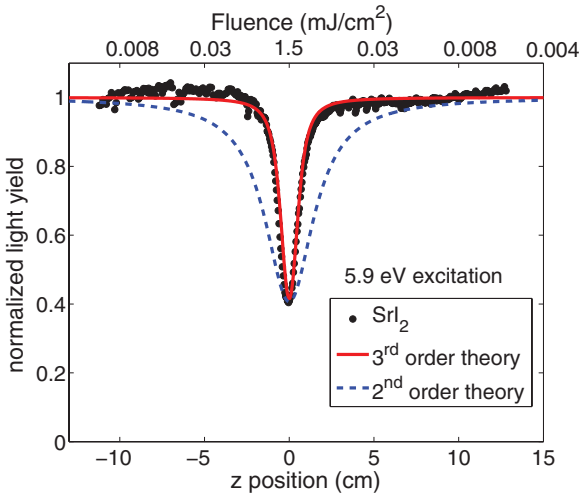

FIG. 6. (Color online) SrI_2 Z-scan data for 5.9-eV excitation (points) fit to third-order quenching (solid line) with $K_3 = 7 \times 10^{-30}$ cm^{6}s^{-1}. The best attempt to fit with second-order kinetics (dashed line) is also shown.

superposition of the raw Z-scan data as long as the Gaussian beam parameters are the same for both. This comparison is made in Fig. 7(a) for SrI_2 and BGO data acquired on the same day with the same 5.9-eV photon energy, beam profile, and externally incident beam power (before reflectance corrections). This makes the empirical difference in kinetic orders very evident.

Up to this point, we have plotted raw data of light yield versus distance z of the beam waist from the entrance surface. Figure 7(b) is a useful alternative way of visualizing the Z-scan data. The format of Fig. 7(b) plots the experimental data as light yield versus the logarithm of excitation density. This plot appears similar to local light yield plots of predicted survival against nonlinear quenching as a function of excitation density that arise in modeling studies of scintillation.[9,33] It can be seen that the experimental light yield curves for both materials in Fig. 7(b) roll off at high excitation density as expected for nonlinear quenching. But the SrI_2 light yield with third-order quenching remains flat longer before finally falling off more steeply compared to BGO having second-order quenching. This is a quite general, straightforward expectation of third- versus second-order kinetics. Third-order quenching turns on later in terms of excitation density. Light yield is flatter for a longer expanse of excitation density in the case of third-order quenching compared to second-order quenching, all else being equal. This has practical significance for the resolution and light yield of SrI_2 relative to BGO, and quite generally for the performance of other scintillators according to whether the dominant quenching kinetics are second or third order. Monte Carlo calculations of energy deposition combined with second- versus third-order quenching confirm that the flatter electron energy response results from third-order kinetics.[33] A second figure of merit for both the sensitivity and the resolution of scintillators is the total light yield. Similar considerations as discussed above lead to the conclusion that the integrated survival against third-order quenching summed over all excitation densities produced by a stopping particle leads to a higher total light yield, compared to the same process

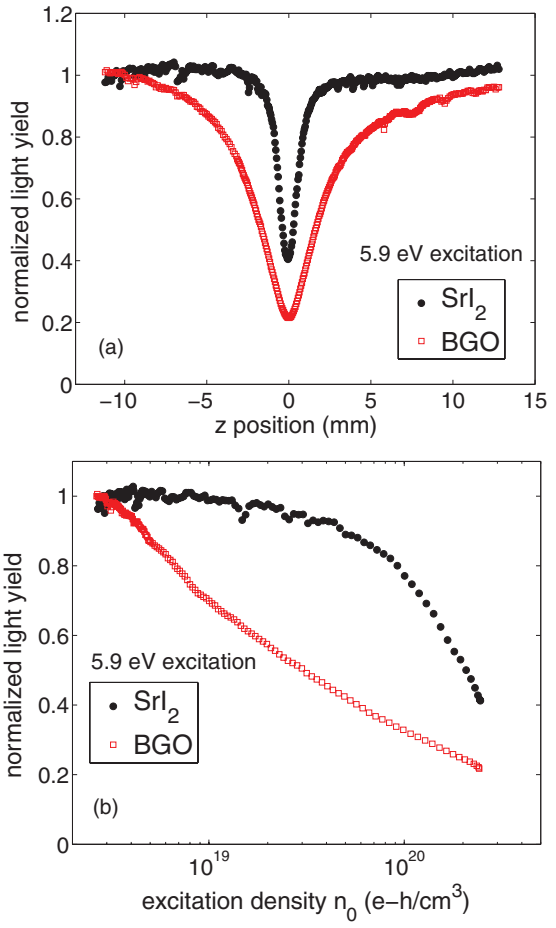

FIG. 7. (Color online) (a) Comparison of BGO (open red squares) and SrI_2 (black points) Z-scan data measured on the same day for the same beam profile, 5.9-eV photon energy, and same external laser beam power. (b) The data are replotted on a logarithmic scale of excitation density for comparing light yield as a function of excitation density in BGO and SrI_2. For this comparison, the absorption coefficient for both crystals was assumed to be the same at $\alpha = 4 \times 10^5$ cm^{-1}, $R(SrI_2) \approx 52\%$ (including sapphire window surfaces), and $R(BGO) \approx 30\%$ (crystal only).

with second-order quenching kinetics as long as the excitation densities produced in an electron track are mostly below the crossing point of the third- and second-order light yield curves [see Fig. 7(b)].

We believe it is worth repeating that Fig. 7(b) summarizes the real differences in performance of both linearity (proportionality) and total light yield resulting from a generic response of a material with dominant third-order quenching, exemplified here by SrI_2, and a material with dominant second-order quenching, exemplified here by BGO.

D. Kinetic order and rate constants of nonlinear quenching in CsI:Tl and NaI:Tl

The free-carrier band gap of CsI at $T = 20$ K has been estimated from the two-photon absorption spectrum to be 6.05 eV.[53] Eby *et al.* measured room-temperature 1s exciton peaks in CsI and NaI at about 5.62 eV and 5.42 eV, respectively.[54] Based on temperature shifts of exciton peaks

in alkali iodides,[54,55] we estimate from the low-temperature two-photon measurement[53] that the room-temperature band gap of CsI should be approximately 5.8 eV. Similar two-photon absorption threshold measurements do not exist for NaI, but the exciton absorption spectra of Eby *et al.*[54] and Teegarden *et al.*[56] establish that the 1*s* exciton peak in NaI is about 0.2 eV lower than in CsI. Combining these temperature and material trends, we estimate a room temperature band gap in NaI of about 5.7 eV, similar to the estimate of 5.8 eV by Rodnyi.[57] Thus within our available fourth harmonic laser photon energy range of 5.9 to 6.1 eV, one finds an interesting transition from creating excitons close to their ionization threshold using 5.9 eV photon excitation, to creating free carriers with about 0.3 to 0.4 eV excess kinetic energy per electron-hole (e-h) pair using 6.1 eV photons. This tuning is observed in the following data to result in a remarkably sharp transition from mixed kinetic order to nearly pure kinetic order of quenching in both CsI:Tl and NaI:Tl. For that reason, the present section is divided into two subsections describing results of excitation at 5.9 and 6.1 eV.

In addition, CsI and NaI have significantly different longitudinal optical phonon frequencies (ω_{LO}), leading to different electron thermalization rates even within the iodide material family. (See Refs. 21–23 and Table I.) Interesting comparisons can be made between data for CsI:Tl and NaI:Tl as the photon energy is changed from 5.9 to 6.1 eV to produce e-h pairs close to their ionization limit at one end and hot (∼300 meV) free carriers at the other. In this section, we present data for the two materials in comparison.

Undoped and lightly Tl-doped CsI data display a positive slope toward the center in the wings of the *Z* scan that appears similar to the semiconductor paradigms introduced earlier in Sec. IV A. For that reason the presentation and analysis of data for undoped CsI and NaI as well as the results of varying Tl concentration to low values will be deferred until Sec. IV F, after the discussion of semiconductor *Z* scans.

1. CsI:Tl and NaI:Tl excited by 5.9-eV photons

Figure 8 shows *Z* scans for CsI:Tl(0.3%), NaI:Tl(0.1%), and BGO measured on the same day with the same laser power and beam profile. As in the previous section on SrI_2, BGO will be included with nearly every new data set as a comparison standard. It is a material with stable surfaces and it has already been established in Sec. IV B that BGO displays nearly pure second-order quenching kinetics for both 5.9 and 6.1 eV photon energy. In Fig. 8, the *Z* scans for NaI:Tl and BGO under 5.9 eV excitation are so nearly coincident that one needs the benefit of color display to distinguish the data points. We can immediately conclude that for 5.9-eV excitation, second-order quenching kinetics prevail in NaI:Tl. From this, we infer either that excitons are directly produced by 5.9-eV photons, albeit in rather highly excited states initially, or that any free carriers produced have negligible excess kinetic energy compared to kT at room temperature and therefore pair to form excitons very rapidly even on the time scale of nonlinear quenching.

The best attempt to fit with a third-order quenching model in Fig. 8, shown by the solid line, is too narrow in the dip to fit any of the experimental data. NaI:Tl excited near the exciton ionization limit is firmly established as a pure case of

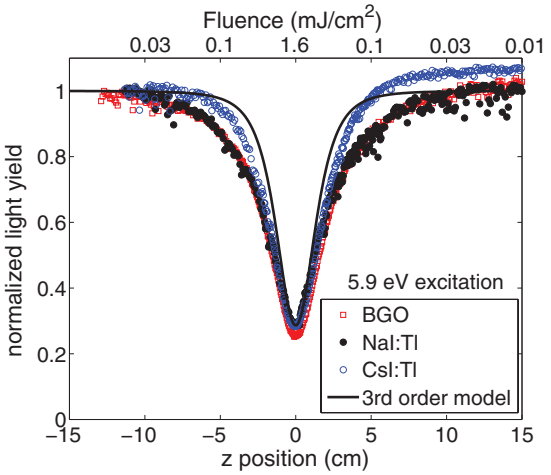

FIG. 8. (Color online) Superimposed *Z*-scan plots of CsI:Tl(0.3%), NaI:Tl(0.1%), and BGO measured with 5.9-eV laser photons on the same day with the same beam profile and same external beam power. External fluence is shown on the top axis. The reflectances are $R(\text{BGO}) = 30\%$, $R(\text{NaI:Tl}) = 16\%$ including quartz windows, and $R(\text{CsI:Tl}) = 7.5\%$. The open red squares for BGO and solid black circular points for NaI:Tl are very closely overlapped to the point of near indistinguishability and both are well fitted by the second-order model as already demonstrated for BGO in Fig. 4.

second-order quenching. However, the CsI:Tl data in Fig. 8 lie intermediate between the second-order real examples and the third-order model curve. CsI:Tl can be fit assuming a mixed population with 45% quenching by second-order and 55% by third-order, as illustrated in Fig. 9.

In summary, this section has presented data on NaI:Tl and CsI:Tl excited with a photon energy (5.9 eV) that creates excitons directly in bound but excited states, or else free carriers with negligible excess kinetic energy in their initial states. The resulting nonlinear quenching kinetics is observed to be pure second order in NaI:Tl under 5.9-eV excitation, and about 45% second order in CsI:Tl. The near coincidence of all three curves at the bottom of the dip in Fig. 8 may make it appear that the data were normalized there. But they were not. Under the same external laser fluence of 2.1 mJ/cm^2 on-axis, these three materials exhibit close to the same total quenching.

2. CsI:Tl and NaI:Tl excited by 6.1-eV photons

Figure 10 shows *Z* scans for CsI:Tl(0.3%), NaI:Tl(0.1%), and BGO excited with 6.1-eV laser photons on the same day with the same laser power and beam profile. (A mixed population fit is illustrated in Fig. 11.) With the exception of the laser photon energy being 6.1 eV, this data set is entirely analogous to that presented for 5.9 eV excitation in Fig. 8. BGO is again a standard of second-order kinetics. A dashed line plots the model of second-order quenching for CsI:Tl and approximately for NaI:Tl data, and the solid line plots the model of third-order quenching for CsI:Tl. The third-order quenching model fits CsI:Tl very well for 6.1-eV photon energy, in marked contrast to the second-order attempted fit (dashed). Recall for comparison that the data for CsI:Tl

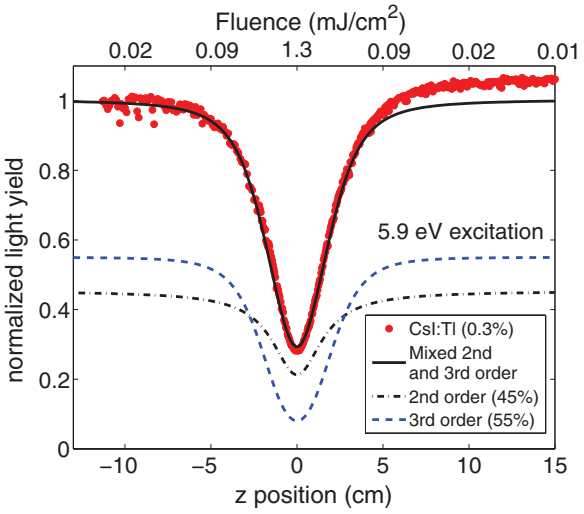

FIG. 9. (Color online) Mixed population model for fitting the Z scan for CsI:Tl(0.3%) excited at 5.9 eV. The room-temperature band gap is estimated to be about 5.8 eV. Since the data lie between the second-order and third-order model curves and examples in Fig. 8, we assume a mixed population model in which 45% of the excitations are excitons quenching in second-order and 55% are free carriers quenching in third-order, with the rate parameters $K_2(t)$ and K_3 as given in Table I. Z-scan predictions for the two-component populations are shown by dashed lines, and their sum by the solid line through the data.

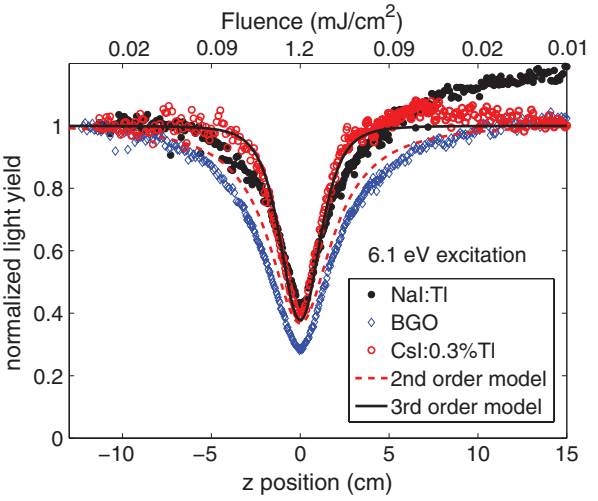

FIG. 10. (Color online) Superimposed Z-scan plots of CsI:Tl(0.3%), NaI:Tl(0.1%), and BGO measured with 6.1-eV laser photons on the same day with the same beam profile and same external beam power. The open blue diamonds for BGO are well fitted by the second-order quenching model as already demonstrated for BGO in Fig. 4(a). The same second-order model for CsI:Tl is shown by the red dashed line and is too wide to fit the data. Rather, the third-order quenching model shown by the solid black line is a good fit to CsI:Tl excited at 6.1 eV. Data for NaI:Tl shown by black solid circles are too wide at the base (top) of the dip to be fit by pure third-order quenching. A mixed population fit is illustrated in Fig. 11. External fluence is labeled on the top axis.

excited at 5.9 eV required a model assuming 45% second-order quenching (see Fig. 9).

The data for NaI:Tl excited at 6.1 eV conform to the third-order quenching model in the central part of the dip, but can be seen in Fig. 10 to be wider at the base (beginning) of the dip than is the third-order model (and the CsI:Tl data). A mixed-population model assuming 65% free carriers (third-order quenching) and 35% excitons (second-order quenching) fits the NaI:Tl data as shown in Fig. 11, except for the previously commented asymmetry artifact between right and left wings.

Under the hypothesis advanced above that 6.1-eV photons excite hot (∼0.3–0.4 eV) carriers in both CsI and NaI, Figs. 8 and 10 would imply that CsI:Tl switches to pure third-order quenching when hot carriers are excited, while NaI:Tl goes only to 65% third-order quenching. Such behavior is consistent with our hypothesis that hot free carriers quench by third-order Auger recombination as long as they remain hot and mobile. When the electrons thermalize after moving some distance from the hole, they are captured preferentially on Tl dopants (at 0.1–0.3% concentration) as Tl^0 separated spatially from the self-trapped hole, and are thus removed from the population subject to nonlinear quenching. The electron capture time to produce Tl^0 in CsI:Tl(0.3%) has been measured as approximately 6 ps[35] and the electron thermalization time is about 7 ps.[21] If a similar capture time exists in NaI:Tl(0.1%), the predicted electron thermalization time of 2 ps in NaI[21] suggests that initially excited hot carriers in that case should spend about half their life free and half their life thermalized (possibly paired with a hole), before finally being scavenged by electron transfer to a Tl dopant.

The hot electron energy relaxation rate given by Refs. 23 and 58 is

$$\tau_{e,\mathrm{LO}}^{-1}(E_e) = \frac{\hbar\Omega_{\mathrm{LO}}\sqrt{m_e^*/m}}{\hbar\tilde{\varepsilon}\sqrt{RyE_e}}\ln\left(\frac{4E_e}{\hbar\Omega_{\mathrm{LO}}}\right) \qquad (15)$$

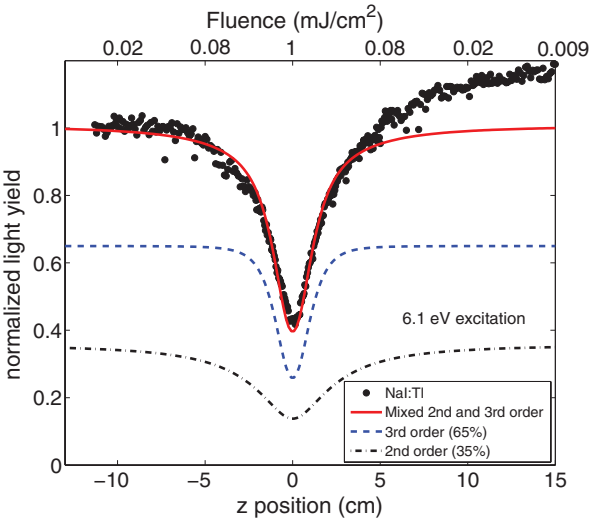

FIG. 11. (Color online) NaI:Tl light yield excited at 6.1 eV with dashed lines showing a population contributing 65% of the normalized maximum yield that quenches by third-order kinetics and a population contributing 35% that quenches by second-order kinetics. The sum of the two dashed line models is the solid curve superimposed on the data.

and depends on the electron energy E_e. $\mathrm{Ry} = e^2/(8\pi\varepsilon_0 a_B) = 13.6$ eV, ε is the effective dielectric permittivity, and m_e^* is the electron effective mass in terms of free electron mass. The time for thermalization of carriers created with only about 300 meV of excess energy such as in NaI and CsI excited by 6.1 eV photons in this experiment will be shorter than the values calculated by Wang *et al.* for electrons starting with several eV energy.[21,22] But the relative thermalization rates in different materials still scale as ω_{LO} according to Eq. (15), so qualitative conclusions based on relative thermalization rates can be drawn.

E. CdTe and CZT

For semiconductor samples in a slab geometry excited close to one surface, we solve the following rate equation including ambipolar diffusion with coefficient D_a (see, e.g., Ref. 59):

$$\frac{\partial n}{\partial t} = D_a \frac{\partial^2 n}{\partial x^2} - An - (B_R + B_{NR})n^2 - K_3 n^3, \qquad (16)$$

subject to the boundary condition at the front surface:

$$D_a \frac{\partial n}{\partial x}\bigg|_{x=0} = -Sn\Theta(n_{\mathrm{sat}} - n) - Sn_{\mathrm{sat}}\Theta(n - n_{\mathrm{sat}}) \qquad (17)$$

and the same boundary condition at a distant (∼2 mm) back surface. The surface recombination velocity is

$$S = \sigma N_s \nu_{\mathrm{th}}, \qquad (18)$$

where N_s is the number of surface recombination centers per unit area, σ is the cross section per center, and ν_{th} is the thermal velocity of transport of the carriers.[60] At saturation, $R_{\mathrm{sat}} = Sn_{\mathrm{sat}}$ is the rate of surface quenching limited by the cycle time of recombination on each quenching site rather than by the arrival rate of diffusing carriers. The use of Heaviside step functions Θ in Eq. (17) marks the transition from fixed S below the threshold n_{sat} to a decreasing surface recombination velocity $S = R_{\mathrm{sat}}/n$ above the threshold of saturation.

Cohen *et al.*[61] have measured a trapping rate on defects $A = (2\ \mathrm{ns})^{-1}$, bulk radiative and nonradiative bimolecular recombination rates, $B_R = 3 \times 10^{-9}\ \mathrm{cm^3 s^{-1}}$, $B_{\mathrm{NR}} \approx 1.1 \times 10^{-9}\ \mathrm{cm^3 s^{-1}}$, and ambipolar diffusion coefficient $D_a = 5\ \mathrm{cm^2/s}$ for CdTe. Surface recombination velocities reported for CdTe vary widely, linked presumably to surface preparation. We took $S = 1 \times 10^5 \mathrm{cm/s}$ in CdTe (see Ref. 62) for the fitting in Fig. 12. There remain just two parameters to be determined from the fitting: the saturation density n_{sat} for surface quenching, and the third-order bulk quenching rate constant K_3. The fitting parameter, K_3 most strongly affects the center of a Z-scan plot while n_{sat} has more effect on the wings, so the fitting can be reasonably specific in determining each of them separately. Their values for the fit shown in Fig. 12 are $K_3 = 5 \times 10^{-30}\ \mathrm{cm^6 s^{-1}}$, $n_{\mathrm{sat}} = 2 \times 10^{19}\ \mathrm{eh/cm^3}$, and therefore $R_{\mathrm{sat}} = 2 \times 10^{24}\ \mathrm{cm^{-2} s^{-1}}$. The fitted value of $K_3 = 5 \times 10^{-30}\ \mathrm{cm^6 s^{-1}}$ in CdTe is comparable to the Auger rate constant $K_3 = 7 \times 10^{-30}\ \mathrm{cm^6 s^{-1}}$ in intrinsic GaAs,[63] another direct gap semiconductor with almost the same band gap as CdTe, consistent with the approximate band gap rule of Auger rates.[38,64]

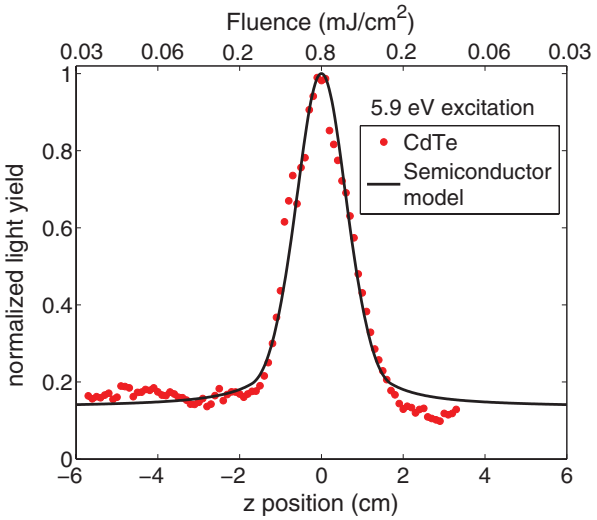

FIG. 12. (Color online) Z-scan data for CdTe excited by 5.9-eV laser photons, normalized at the highest light yield ($z = 0$). The solid curve is the model discussed in this section, taking into account bimolecular radiative and nonradiative decay with published rate constants, third-order Auger quenching, linear trapping on defects, and diffusion into the bulk and to the surface where surface quenching may occur at a saturable rate. Fluence axis includes correction for reflectance $R = 20\%$.

F. Undoped CsI and variation of Tl concentration

We have delayed the presentation of data on undoped or lightly Tl-doped CsI until after the discussion of semiconductors in the previous section. It can be seen in Fig. 13 that undoped CsI exhibits wings sloping upward toward the center, suggestive of the behavior seen in CdTe and especially resembling the ZnO Z scan shown in Fig. 3. The BGO reference standard illustrates pure second-order quenching, and the Z scan for CsI:Tl(0.3%), shown with black circular points, fits a mixed model as discussed in regard to Fig. 8.

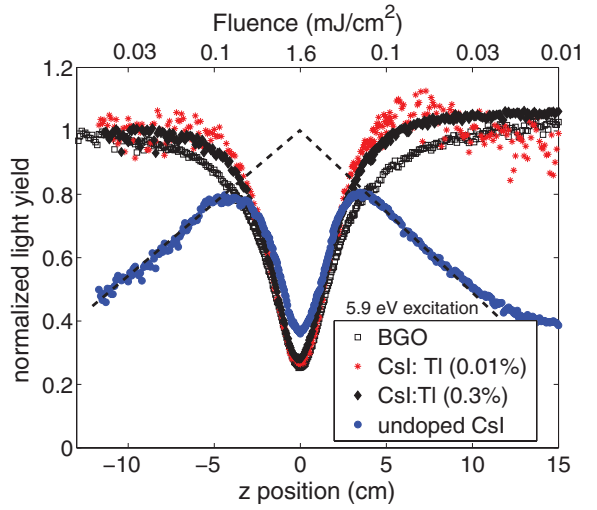

FIG. 13. (Color online) Superposition of Z scans for CsI:Tl(0.3%), CsI:Tl(0.01%), undoped CsI, and BGO measured on the same day with 5.9-eV photon energy, same beam profile, and same external beam power.

The wings acquire an upward slope toward the center as Tl concentration decreases from 0.3%, with the slope becoming very pronounced in undoped CsI.

As commented for CdTe in the previous section, the positive sloping wings will generally be encountered when there is a quenching channel having kinetics at least one order lower than the radiative kinetic order. The saturable surface quenching discussed in Sec. IV E is one such possibility when the radiative decay is first order, such as for excitons excited at 5.9 eV in CsI. Nagata *et al.*[31] have discussed experimental evidence for STE diffusion to surface quenchers in NaI, and we have interpreted shortened STE lifetime in uv-excited CsI relative to the bulk on such a basis.[10]

The normalization point of the Z-scan curves becomes a practical consideration for interpreting the amount of nonlinear quenching in the case of sloping wings. In plotting and fitting BGO, $CdWO_4$, SrI_2, CsI:Tl(0.3%), and NaI:Tl(0.1%), normalization to maximum light yield was defined in the far left wing at $z = -12$ cm because the light yield reaches its maximum value at the lowest excitation density in those cases. In materials such as CdTe, ZnO, and undoped CsI, that is no longer the case. We have normalized at the intersection point of the projections of the sloping wings to $z = 0$ as illustrated by the dashed line extrapolations in Fig. 13. The assumption is that this would be the maximum light yield versus z if nonlinear quenching were turned off. The dependence of the central quenching dip on the concentration of Tl dopant in the range 0.01% to 0.3% for 5.9 eV excitation is shown in Supplemental Material.[65]

Figure 14 shows an overlay of undoped CsI and BGO data measured with 6.1-eV laser photons rather than 5.9 eV. These data are also normalized at the $z = 0$ intersection of extrapolated wings. The central dip fits third-order quenching for 6.1-eV photon energy, in agreement with the CsI:Tl(0.3%) results in Sec. IV D2. BGO illustrates pure second-order kinetics.

In a future publication, we will show experimental Z-scan data in which the SrI_2:Eu system exhibits an interesting reversal of the trend described above for CsI and CsI:Tl. Undoped SrI_2 does not exhibit sloping of the wings, but doping SrI_2 with europium introduces upward sloping wings in the Z scan reminiscent of undoped CsI shown in Fig. 13. The central dip in SrI_2 remains third-order regardless of whether there is europium or not.

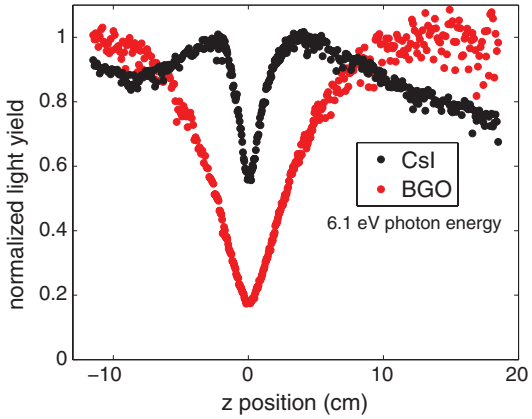

FIG. 14. (Color online) Undoped CsI and BGO are compared for 6.1-eV photon energy, same beam profile and similar external beam power.

G. Experimental determination of the track-end quenching radius

The radius of the ionization track produced by a high-energy electron is an important physical parameter in modeling diffusion and quenching dynamics in scintillators, but experimental measurements of the track radius have seemed difficult. Nonlinear quenching rates are proportional to powers of the volumetric excitation densities n (eh/cm^3), rather than powers of the linear spatial rate of energy deposition from a high-energy electron, dE/dx (eV/cm). A commonly used formula for converting dE/dx to excitations per unit volume, n, assumes a Gaussian cylindrical track of $1/e$ radius r_{track} and expresses the average energy invested to create each electron-hole pair as βE_{gap}:

$$n = \frac{{}^{dE}/_{dx}}{\beta E_{\text{gap}} \int_0^{2\pi} d\phi \int_0^{\infty} r \exp\left(-r^2/r_{\text{track}}^2\right) dr}. \tag{19}$$

This reduces to

$$n = \frac{{}^{dE}/_{dx}}{\beta E_{\text{gap}} \pi r_{\text{track}}^2} \tag{20}$$

after integrating the denominator. Regardless of the actual track shape, the square of a length is required in the denominator for dimensional reasons. The second and third powers of N and n appearing in Eqs. (7) and (3), respectively, mean that the track radius appears in fourth or sixth power in the appropriate rate equation. Since the track radius can expand significantly due to diffusion in such a large gradient, carrier mobilities may be expected to have a significant effect on nonlinear quenching, scintillator proportionality, and light yield.[9–12,24,33]

Until this work[66–68] and the concurrent work of Laasner *et al.*,[19] the electron track radius in a scintillator had not been experimentally determined. The tracks are stochastic in location and time, so direct imaging is very difficult. However, indirect determination is possible. The laser fluence in a Z-scan experiment can be adjusted to produce the same nonlinear quenching at the bottom of the dip as is seen in K-dip spectroscopy at a track-end value of electron energy (e.g., 80 eV) in NaI:Tl. Briefly, K-dip spectroscopy analyzes the light yield attributable to excitation by K-shell photoelectrons of specific energy selected by tuning synchrotron radiation relative to the K edge.[15] It is assumed that the same excitation density n_0 will produce the same amount of nonlinear quenching in each of the two experiments compared in Fig. 15. We equate the peak densities n_0 expressed in Eqs. (2) and (20) and solve for r_{NLQ}, the effective radius in which nonlinear quenching occurs:

$$r_{\text{NLQ}}^2 = \frac{h\nu({}^{dE}/_{dx})}{F_0 \alpha \beta E_{\text{gap}} \pi}. \tag{21}$$

The result in NaI:Tl with $\alpha = 4 \times 10^5$ eh/cm^3 (see Ref. 58), $F_0 = 0.4$ mJ/cm^2, $h\nu = 5.9$ eV, dE/dx (at 80 eV) = 64 eV/nm (see Ref. 8), $\beta = 2.5$ (see Ref. 5), and $E_{\text{gap}} = 5.7$ eV is $r_{\text{NLQ}} \approx 3$ nm near the track end. Using the NWEGRIM

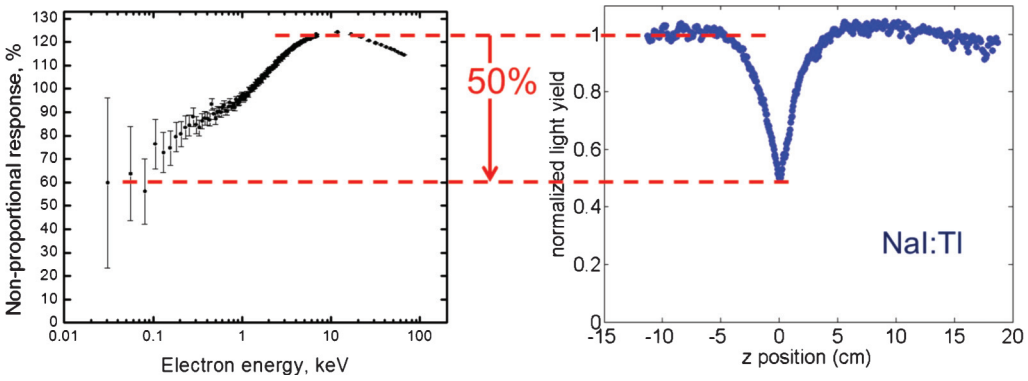

FIG. 15. (Color online) K-dip spectroscopy for NaI:Tl (Ref. 15) (left) with 50% quenching near the track end. On the right are the Z-scan results for NaI:Tl with the uv laser fluence tuned to produce the same level of quenching, thus determining the required excitation density n_0.

Monte Carlo code, Gao *et al*. have calculated the radius of the self-trapped hole distribution at track end in NaI to be 2.8 nm.[69]

H. Tabulation of kinetic order, total nonlinear quenching, and rate constants in insulators

Table I presents a summary, for the wide gap materials studied, of the observed kinetic order of nonlinear quenching, the total nonlinear quenched fraction $QF(n_0)$ at a standard excitation density $n_0 = 1 \times 10^{20}$eh/cm^3, and the rate constants κ_2 and K_3 for second-and third-order quenching. Values are listed separately for 5.9-eV and 6.1-eV laser photon energy. Also listed are the electronic band gap E_g for free carrier production, the highest zone-center longitudinal optical phonon frequency $\omega_{\rm LO}$, and the calculated or estimated electron thermalization time, $\tau_{\rm th}$, with source references as

TABLE I. For 5.9-eV and 6.1-eV photon energy, respectively, measured values of the kinetic order of nonlinear quenching (NLQ), the total nonlinear quenched fraction $QF(n_0)$ at a standard excitation density $n_0 = 1 \times 10^{20}$ eh/cm^3, and the rate constants κ_2 and K_3 for second- and third-order quenching are listed for insulators studied in this work. Also listed are the room-temperature band gap E_g, approximate absorption coefficient α at 6 eV, the highest zone center longitudinal optical phonon frequency $\omega_{\rm LO}$, and the calculated or estimated electron thermalization time, $\tau_{\rm th}$.

		5.9 eV excitation				6.1 eV excitation						
Crystal	E_g(eV)	Order of NLQ	$QF(n_0)$	κ_2 10^{-15} (cm^{3}s$^{-1/2}$)	K_3 10^{-29} (cm^{6}s^{-1})	Order of NLQ	$QF(n_0)$	κ_2 10^{-15} (cm^{3}s$^{-1/2}$)	K_3 10^{-29} (cm^{6}s^{-1})	α 10^5 (cm^{-1})	$\omega_{\rm LO}$ 10^{13} (s^{-1})	$\tau_{\rm th}$ (ps)
BGO	4.2[a]	2	0.59	0.01	NA	2	0.593	0.01	NA	5.6[b]	15.3[c]	$\leqslant$0.5
$CdWO_4$	4.8[d]	2	0.52	0.003	NA	2	0.52	0.0029	NA	9.6[e]	17.3[f]	$\leqslant$0.5
SrI_2	5.5[g]	3	0.23	NA	0.7	3	0.24	NA	0.73	4	2.6[h]	4
CsI:Tl	5.8[i]	2@45% 3@65%	0.47	1.7	6.6	3	0.41	NA	6.6	2.7[j]	1.79[k]	7[l]
NaI:Tl	5.7[m]	2	0.36	2.3 0.8	NA	2@35% 3@65%	0.33	2.3 0.8	3.2	4[n]	3.47[o]	2[p]
CsI	5.8[i]	...	0.46	$\leqslant$0.8	...	3	0.37	NA	4.5	2.7[j]	1.79[k]	7[l]

[a]Reference 48.
[b]References 48 and 70.
[c]Reference 71.
[d]References 49 and 50.
[e]Reference 72.
[f]Reference 73.
[g]Reference 74.
[h]Reference 75.
[i]References 53, 55 and 56.
[j]Reference 10.
[k]Reference 29.
[l]Reference 22.
[m]References 54, 55 and 57.
[n]Reference 55.
[o]Reference 29.
[p]Reference 22.

superscripts. The absorption coefficient data are generally not precise enough to warrant distinguishing α at 5.9 and 6.1 eV for room temperature, so the single α value listed was used for both. The sequencing of the columns for kinetic order of nonlinear quenching, total nonlinear quenched fraction $QF(n_0)$, and the rate constants κ_2, K_3 reflects the increasing amount of additional analysis and data needed to extract the latter numbers. The kinetic order comes directly from the shape of the fitted data, whereas the conversion to excitation density n_0 for specifying $QF(n_0)$ requires knowledge of absorption coefficient, and extraction of the rate constants requires model assumptions and competing rates described in Sec. III B. For example, two values of κ_2 are reported for NaI:Tl(0.1%) in Table I, corresponding to two choices of the scavenging rate constant S_{1e} in Eq. (11) used for fitting. The values of S_{1e} for CsI:Tl(0.3%) and CsI:Tl(0.01%) were measured experimentally as $(6\ \text{ps})^{-1}$ and $(100\ \text{ps})^{-1}$ respectively.[35] Values for S_{1e} in NaI:Tl(0.1%) have not yet been measured. The reported $\kappa_2 = 2.3 \times 10^{-15}\ \text{cm}^3\text{s}^{-1/2}$ assumes S_{1e} the same as in CsI:Tl(0.3%), whereas the value $\kappa_2 = 0.8 \times 10^{-15}\ \text{cm}^3\text{s}^{-1/2}$ is obtained assuming $S_{1e} = (71\ \text{ps})^{-1}$ the same as for CsI:Tl(0.1%) obtained by linear interpolation of capture rate versus trap concentration. In Table I, NA signifies that a population quenching by the corresponding kinetic order was not produced significantly by the photon energy used.

Several trends and general behaviors can be seen in Table I. For example, the total nonlinear quenched fraction $QF(n_0)$ evaluated at $n_0 = 10^{20}\ \text{eh/cm}^3$ changes by little more than a factor 2 across the whole set of five oxide and iodide materials listed in Table I. This seems a remarkable degree of constancy for a nonlinear response surveyed across five different insulators that are known to include variously second-order and third-order quenching kinetics. It seems especially remarkable considering that in the series of second-order quenching materials from $CdWO_4$ to BGO to NaI:Tl and CsI:Tl (specifically with excitons created by 5.9-eV light), the extracted rate constants κ_2 vary by three orders of magnitude. Across the same set of materials, the radiative lifetimes of self-trapped excitons (STE) also span three decades, reflecting the larger spin-orbit mixing of singlet and triplet character in the iodides compared to the oxides. Equation (6) gives a reason for expecting a dependence of κ_2 on $\tau_R^{-1/2}$ if R_{dd} remained constant. But the correlation between κ_2 and τ_R in Table I is stronger than that. The empirical finding of little variation in $QF(n_0)$ among these materials implies a roughly inverse correlation of κ_2 and τ_R simply because τ_R, as the main 1st order competing channel, sets the effective time interval over which κ_2 can act to accomplish $QF(n_0)$.

From measured κ_2 and the radiative lifetime τ_R, Eq. (6) allows extraction of the Förster transfer radius R_{dd} listed in Table II. The primary experimental observation of nearly constant $QF(n_0)$ among the second-order measurements, together with the wide variation of radiative lifetimes τ_R between the oxides and alkali iodides, leads to the finding of significantly larger R_{dd} in the alkali iodides compared to the two oxides. Several R_{dd} values measured by the method of decay time dependence on excitation density are listed for comparison and labeled R'_{dd} in the last column of Table II. R_{dd} and R'_{dd} should be the same regardless of measurement method, but the two different methods of experiments and analyses have different challenges and assumptions leading to possible error.

Based on the limited survey of five insulators with accessible band gaps in our experiment, we have found that the total amount of nonlinear quenching, $QF(n_0)$, at excitation density $10^{20}\ \text{eh/cm}^3$ corresponding approximately to the end of an electron track does not seem to depend sensitively on the magnitude of κ_2 or K_3, even when κ_2 varies by three decades.

TABLE II. For the four materials exhibiting second-order quenching (under appropriate photon energy), the second-order quenching rate constant, κ_2, the self-trapped exciton radiative lifetime τ_R, and the deduced Förster transfer radius R_{dd} are listed. The last column lists R'_{dd} deduced from the alternative method of decay time versus excitation density.

Crystal	Photon energy (eV)	κ_2 ($10^{-15}\ \text{cm}^3\text{s}^{-1/2}$)	τ_R (ns)	R_{dd} (nm)	R'_{dd} (nm)
$CdWO_4$	5.9 6.1	0.003	15 000[a]	1.5	2.1 ± 0.15[f] 3[g] 3.7[h]
BGO	5.9 6.1	0.01	300[b]	1.14	...
CsI:Tl	5.9	1.7	15[c] 1.4[d]	3.8	4.3 2.9[i]
NaI:Tl	5.9	2.3 0.8	13[e]	4.1 2.9	...

[a]Reference 17.
[b]Reference 76.
[c]Reference 45.
[d]Reference 10.
[e]Reference 77.
[f]Reference 17.
[g]Reference 18.
[h]Reference 19.
[i]Reference 10.

$QF(n_0)$ at this n_0 does not even depend very much on whether the quenching is second or third order. The total $QF(n_0)$ in SrI_2 with third-order quenching kinetics is the smallest one among all $QF(n_0)$ listed in Table I. In fact, if it were not for SrI_2, the standard deviation of $QF(n_0)$ among the remaining four insulators is very small indeed, at just 8.5%. So another way of stating this generalization from a modest sample of oxide and iodide materials is that the nonproportionality of a scintillator has only weak sublinear dependence on the second-order rate constant κ_2, in particular. Part of the reason is simply the self-terminating nature of nonlinear quenching. A small rate constant K does not deplete the excited population as quickly, so it acts on a higher average population for the duration permitted by competing rates, compared to the case with a larger nonlinear K. The resulting trend is that total quenched fraction tends to depend sublinearly on the rate constant for nonlinear quenching.

SrI_2, the material with the lowest total $QF(n_0)$ in our whole insulator group, exhibits pure third-order quenching and is indeed the empirical best-performing scintillator. Part of the outstanding proportionality and light yield of SrI_2:Eu among scintillators must be attributable to the fact that its Auger rate constant K_3 is about five times lower than the value found in the alkali iodides in Table I. Another part of its good performance is the very fact of third-order rather than second-order quenching, as already discussed in regard to Fig. 7(b). Yet a third reason for the good performance of SrI_2 relative to NaI is based on hot electron diffusion.[25]

Table III lists Auger rate constants K_3 measured in this Z-scan experiment on iodide insulators and CdTe, in comparison to published Auger rate constants in narrow-gap and wide-gap semiconductors measured by reflectivity[39] and photoluminescence,[63,78] respectively.

Figure 16 plots the Auger rate constants versus band gap on a log-log scale. The semiconductors form a sloping line expressing a general band gap rule of decreasing Auger rate versus increasing band gap. The K_3 for CdTe from Z scan falls on the trend line, but the alkali iodide rate constants measured in this work are about two decades above the trend line and SrI_2 is about one decade above.

TABLE III. Measured Auger rate constants K_3 (cm^6s^{-1}) reported in the literature or determined from the present Z-scan experiments are listed for direct-gap semiconductors and iodide insulators along with room-temperature band gaps E_g (eV) and optical phonon frequency $\omega_{LO}(s^{-1})$. Measurements are at room temperature.

Crystal	K_3 (cm^6s^{-1}) $\times 10^{-29}$	Reference	E_g(eV)	ω_{LO} (s^{-1}) $\times 10^{13}$
InSb	1200	39	0.17	3.7
GaSb	7	39	0.7	4.3
GaAs	0.7	63	1.43	5
CdTe	0.5	Z scan	1.44	3.1
$In_{0.15}Ga_{0.85}N$	0.2	78	2.64	14
$In_{0.09}Ga_{0.91}N$	0.14	78	2.83	14
SrI_2	0.7	Z scan	5.5	2.6
NaI:Tl	3.2	Z scan	5.7	3.47
CsI:Tl	6.6	Z scan	5.8	1.79
CsI	4.5	Z scan	5.8	1.79

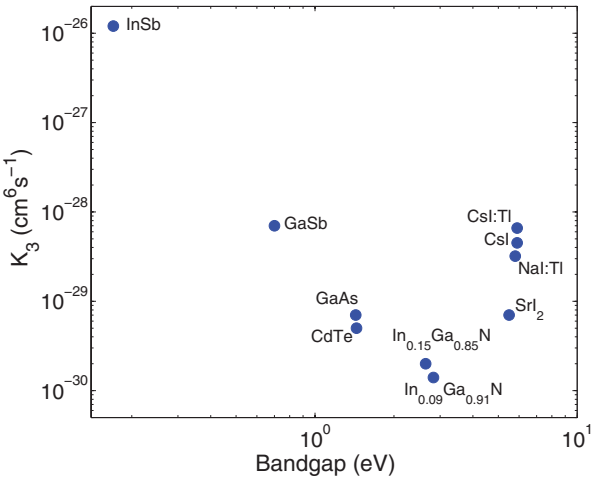

FIG. 16. (Color online) Auger recombination rate constant K_3 (cm^6s^{-1}) plotted vs band gap (eV) for the materials in Table III.

There are at least two interpretations of Fig. 16 that can be given. The first accepts the premise of our Auger quenching rate analysis expressed in Eq. (8). In order to account for finding third-order quenching in the iodides versus second-order quenching in the oxides, we assumed that the slow electron thermalization characteristic of iodides dictates that the free carrier population will dominate during nonlinear quenching. The purity of third-order kinetics observed in the iodides implies within this hypothesis that nonlinear quenching occurs mainly within the electron thermalization time in iodides. This is taken as roughly 6 ps in Eq. (8) for use in data analysis. In this interpretation, the enhanced Auger rate constant in iodides is a real effect attributable to the carriers remaining out of equilibrium with the lattice, possessing up to 300 meV excess kinetic energy (up to 3500 K electron temperature) in alkali iodides and up to 0.6 eV in SrI_2 in the 6.1 eV Z-scan experiments. It is known that lattice temperature accelerates Auger recombination particularly in wide-gap materials. As the energy of e-h recombination given to the spectator electron (or hole) increases, the final state momentum needed to conserve energy tends to exceed the total momentum that was available in the initial state. This accounts very qualitatively for the band gap rule of Auger rates. At high lattice temperature, phonons can provide the needed momentum in indirect Auger events. Excess electron temperature should also increase the probability of conserving momentum for large energy transfers in Auger recombination. Although moderately hot electrons do not possess mean momenta as large as phonons, neither do hot carriers as sources of momentum represent a fourth participant (phonon) as in indirect Auger processes. A numerical assessment is outside the scope of the present paper, but we suggest this hypothesis as a way to reconcile the behavior observed in Fig. 16 with the hot-electron explanation of finding third-order quenching specifically in iodides.

The alternate interpretation would be that the premise of Eq. (8) and its surrounding discussion is wrong, and that the free-carrier Auger (third-order) quenching continues well beyond the time limit imposed by carrier cooling and trapping. If the integration of Auger decay extends about two decades longer than assumed in Eq. (8), then analysis of

the Z-scan data could yield K_3 values more in line with the qualitative band gap trend of Fig. 16. But then we would have to look elsewhere than hot electron thermalization to resolve the observed third-order/second-order dichotomy of iodides versus oxides and to account for the sharp change in kinetic order upon tuning photon energy only 200 meV higher above the band gap in iodides. We have not found an alternative explanation for the latter observations.

V. CONCLUSIONS

The first striking conclusion that emerges from these experiments is that in the oxide and iodide insulators studied so far, the kinetic order of nonlinear quenching is nearly pure second order in the oxides and nearly pure third order in the iodides when excited well above the band gap. There is good reason to expect free-carrier kinetics, including third-order Auger quenching, in semiconductors having exciton binding energies less than or equal to kT. But insulators such as the oxides and iodides studied in this work have exciton binding energies of typically 0.3 eV,[53,79] much larger than kT at room temperature. Why then are third-order quenching kinetics of free-carrier Auger decay found to be dominant in the iodide insulators? Conversely, why is that not the case in the oxide insulators studied, having comparable exciton binding energy?

We have suggested that the difference is based on electron thermalization time and its dependence on LO phonon frequency, as calculated by Wang *et al.*[21,22] and Kirkin *et al.*,[23] for example. Representative thermalization times τ_{th} for hot electrons with excess energy of a few eV are listed in Table I for comparison to the observed order of nonlinear quenching. A correlation seems clear. Even the exception to the general iodide/oxide rule, i.e., the finding of a mixture of quenching orders in NaI:Tl when hot free carriers are excited by 6.1-eV laser photons, makes sense in these terms. In NaI, the representative electron thermalization time is 2 ps, midway between the slow ($\sim$7 ps) thermalization in CsI and the prompt ($\leqslant$0.5 ps) thermalization in oxides. Since the main part of nonlinear quenching and the thermalization of hot electrons both appear to take place on picosecond time scales, the kinetic order of nonlinear quenching could depend on which process takes place faster.

In contrast to the weak dependence on κ_2 noted in the previous section, there is a big empirical change in the amount of nonlinear quenching $QF(n_0)$ in going from insulators to semiconductors within our sample of eight materials. One sees deep quenching dips in the Z scans of all the insulators, a much attenuated dip for the moderate-mobility semiconductor ZnO, and no quenching dip discernible to the eye in Z scans of the good semiconductors CdTe and CZT. In effect, the Z-scan experiment has given a direct empirical confirmation of what we demonstrated previously by numerical modeling of diffusion and nonlinear quenching in the two materials CsI:Tl and high-purity Germanium.[10,14] The numerical model was based on competition between diffusion of excitations (carriers) to reduce their density in the track core, and nonlinear quenching which depends on excitation density. In the Z-scan experiment, there is no particle track, but diffusion out of the thin uv absorption layer plays the same competitive role with the nonlinear quenching in a one-dimensional slab geometry. This competition between diffusion and nonlinear quenching can be seen by comparing the Z-scan data for semiconductors and insulators. Diffusion should be an even more successful competitor for lowering the core density n_0 in an electron track of roughly 3-nm radius.

In summary, whereas the total nonlinear quenching QF depends sublinearly on κ_2 or K_3 (see Table I), it should scale roughly with the inverse second or third power of ambipolar diffusion coefficient in a cylindrical electron track, and inverse first or 1.5 power in a slab geometry due to dependence of quenching rate on n^2 or n^3. Thus the empirical results spanning insulators and semiconductors, and the expected parameter dependence of competition between nonlinear quenching and dilution by diffusion support the emerging recognition of the role of excitation diffusion in electron tracks and its consequences for the proportionality of electron energy response.[9–12,16,23–25,34]

It still remains that quantitative rate constants for nonlinear quenching are needed for model simulations of light yield. The experimental electron energy response or light yield as a function of the initial energy of the electron, $Y_L(E_i)$, can be measured by Compton-coincidence spectroscopy (e.g., SLYNCI)[6,36,80] and K-dip spectroscopy.[15] The predicted electron energy response of NaI:Tl and SrI_2:Eu with K_3 and r_{track} measured in this work and other data taken from the literature or estimated from similar materials has been compared to Compton coincidence and K-dip experiments.[33] Note that although values of $K_2(t)$ could be measured in alkali iodides in this experiment if the laser photon energy created excitons directly, it is only K_3 that will be relevant to the excitation spectrum in a high-energy electron track. As reported in Ref. 33, reasonably good agreement with both Compton coincidence[80] and K-dip experiments[15,81] was found in NaI:Tl and SrI_2:Eu using K_3 measured by these Z-scan experiments.

It is also useful to conduct microscopic numerical modeling of the Z-scan experiment itself. Wang, *et al.* have conducted kinetic Monte Carlo (KMC) modeling of the present Z-scan experiments on CsI and CsI:Tl.[65] The simpler and better determined spatial distribution and excitation energy distribution of laser photo-excitation of a slab rather than the stochastic complexities of an electron track make it possible to benchmark and refine parameters in the Monte Carlo model, which can then be applied in simulations of electron tracks. Initial results of the KMC simulations of second-order quenching and light yield in CsI:Tl and NaI:Tl Z scans excited at 5.9 eV are reported in Refs. 65 and 82, respectively.

We have already noted that the limit of laser harmonic photon energy currently available in our laboratory, i.e., 6.1 eV, limits the range of accessible band gaps for these measurements. However, the use of other pulsed ultraviolet sources such as free-electron laser, storage ring undulator, or high harmonic laser conversion should be able to extend this method to wider gap materials in future work. Indeed, the first work on nonlinear quenching in a scintillator by the decay time method used a high harmonic laser source.[17] Extending the interband Z-scan survey to a wide range of material band gaps should be possible, interesting, and useful.

ACKNOWLEDGMENTS

Supported by the National Nuclear Security Administration, Office of Nonproliferation Research and Development

(NA-22) of the US Department of Energy under Contracts DE-NA0001012 and DE-AC02-05CH11231. We thank Sebastien Kerisit and Fei Gao (Pacific Northwest National Laboratory), Andrey Vasilev (Moscow State University), and Qi Li (Wake Forest University) for helpful discussions particularly of hot electron thermalization and quenching phenomena.

*grimjq@wfu.edu
†williams@wfu.edu

[1]M.-H. Kim, M. F. Schubert, Q. Dai, J. K. Kim, E. F. Schubert, J. Piprek, and Y. Park, Appl. Phys. Lett. **91**, 183507 (2007).
[2]E. Kioupakis, P. Rinke, K. T. Delaney, and C. G. V. de Walle, Appl. Phys. Lett. **98**, 161107 (2011).
[3]N. F. Gardner, G. O. Müller, Y. C. Shen, G. Chen, S. Watanabe, W. Götz, and M. R. Krames, Appl. Phys. Lett. **91**, 243506 (2007).
[4]W. W. Moses, G. A. Bizarri, R. T. Williams, S. A. Payne, A. N. Vasil'ev, J. Singh, Q. Li, J. Q. Grim, and W. Choong, IEEE Trans. Nucl. Sci. **59**, 2038 (2012).
[5]P. Dorenbos, IEEE Trans. Nucl. Sci. **57**, 1162 (2010).
[6]S. Payne, N. Cherepy, G. Hull, J. Valentine, W. Moses, and W.-S. Choong, IEEE Trans. Nucl. Sci. **56**, 2506 (2009).
[7]J. Jaffe, D. Jordan, and A. Peurrung, Nucl. Instrum. Meth. A **570**, 72 (2007).
[8]G. A. Bizarri, W. W. Moses, J. Singh, A. N. Vasil'ev, and R. T. Williams, J. Appl. Phys. **105**, 044507 (2009).
[9]Q. Li, J. Q. Grim, R. T. Williams, G. A. Bizarri, and W. W. Moses, J. Appl. Phys. **109**, 123716 (2011).
[10]R. T. Williams, J. Q. Grim, Q. Li, K. B. Ucer, and W. W. Moses, Phys. Status Solidi B **248**, 426 (2011).
[11]I. Khodyuk and P. Dorenbos, IEEE Trans. Nucl. Sci. **59**, 3320 (2012).
[12]J. Singh and A. Koblov, IEEE Trans. Nucl. Sci. **59**, 2045 (2012).
[13]M. Moszynski, J. Zalipska, M. Balcerzyk, M. Kapusta, W. Mengesha, and J. Valentine, Nucl. Instrum. Meth. A **484**, 259 (2002).
[14]Q. Li, J. Q. Grim, R. T. Williams, G. A. Bizarri, and W. W. Moses, Nucl. Instrum. Meth. A **652**, 288 (2011).
[15]I. V. Khodyuk, P. A. Rodnyi, and P. Dorenbos, J. Appl. Phys. **107**, 113513 (2010).
[16]M. Nikl, J. A. Mares, M. Dusek, P. Lecoq, I. Dafinei, E. Auffray, G. P. Pazzi, P. Fabeni, J. Jindra, and Z. Skoda, J. Phys.: Condens. Matter **7**, 6355 (1995).
[17]M. Kirm, V. Nagirnyi, E. Feldbach, M. De Grazia, B. Carré, H. Merdji, S. Guizard, G. Geoffroy, J. Gaudin, N. Fedorov, P. Martin, A. Vasil'ev, and A. Belsky, Phys. Rev. B **79**, 233103 (2009).
[18]V. Nagirnyi, S. Dolgov, R. Grigonis, M. Kirm, L. Nagornaya, F. Savikhin, V. Sirutkaitis, S. Vielhauer, and A. Vasil'ev, IEEE Trans. Nucl. Sci. **57**, 1182 (2010).
[19]R. Laasner, V. Nagirnyi, S. Vielhauer, M. Kirm, S. Markov, A. V. V. Makhov, V. Sirutkaitis, R. Grigonis, N. Fedorov, and S. Guizard (private communication).
[20]J. Q. Grim, Q. Li, K. B. Ucer, R. T. Williams, and W. W. Moses, Nucl. Instrum. Meth. A **652**, 284 (2011).
[21]Z. Wang, Y. Xie, B. D. Cannon, L. W. Campbell, F. Gao, and S. Kerisit, J. Appl. Phys. **110**, 064903 (2011).
[22]Z. Wang, Y. Xie, L. W. Campbell, F. Gao, and S. Kerisit, J. Appl. Phys. **112**, 014906 (2012).
[23]R. Kirkin, V. Mikhailin, and A. Vasil'ev, IEEE Trans. Nucl. Sci. **59**, 2057 (2012).
[24]A. Kozorezov, J. K. Wigmore, and A. Owens, J. Appl. Phys. **112**, 053709 (2012).
[25]Q. Li, J. Q. Grim, K. B. Ucer, A. Burger, G. A. Bizarri, W. W. Moses, and R. T. Williams, Phys. Status Solidi RRL **6**, 346 (2012).
[26]*Characterization Techniques and Tabulations for Organic Nonlinear Materials*, 1st ed. (Marcel Dekker, Inc., New York, 1998), pp. 655–692.
[27]M. Sheik-bahae, A. A. Said, and E. W. V. Stryland, Opt. Lett. **14**, 955 (1989).
[28]See Supplemental Material at http://link.aps.org/supplemental/10.1103/PhysRevB.87.125117 for images of the beam profile, a more detailed description of the reasons lattice heating is not responsible for the *Z*-scan response, and CsI:Tl *Z*-scan plots for a range of Tl concentrations.
[29]K. S. Song and R. T. Williams, *Self-trapped Excitons*, 2nd ed. (Springer-Verlag, Heidelberg, 1996).
[30]X. Yu and A. M. Hofmeister, J. Appl. Phys. **109**, 033516 (2011).
[31]S. Nagata, K. Fujiwara, and H. Nishimura, J. Lumin. **47**, 147 (1990).
[32]V. B. Mikhailik, H. Kraus, S. Henry, and A. J. B. Tolhurst, Phys. Rev. B **75**, 184308 (2007).
[33]J. Q. Grim, Q. Li, K. B. Ucer, R. T. Williams, G. A. Bizarri, and W. W. Moses, MRS Commun. **2**, 139 (2012).
[34]J. Q. Grim, Q. Li, K. B. Ucer, A. Burger, G. A. Bizarri, W. W. Moses, and R. T. Williams, Phys. Status Solidi A **209**, 2421 (2012).
[35]R. T. Williams, K. B. Ucer, J. Q. Grim, K. C. Lipke, L. M. Trefilova, and W. W. Moses, IEEE Trans. Nucl. Sci. **57**, 1187 (2010).
[36]S. Payne, W. Moses, S. Sheets, L. Ahle, N. Cherepy, B. Sturm, S. Dazeley, G. Bizarri, and W.-S. Choong, IEEE Trans. Nucl. Sci. **58**, 3392 (2011).
[37]A. Vasil'ev, in *Proceedings of the 8th International Conference on Inorganic Scintillators and their Applications (SCINT 2005)*, edited by A. Gektin and B. Grinyov (National Academy of Sciences of Ukraine, Kharkov, 2006), pp. 1–6.
[38]V. Chazapis, H. A. Blom, K. L. Vodopyanov, A. G. Norman, and C. C. Phillips, Phys. Rev. B **52**, 2516 (1995).
[39]S. Marchetti, M. Martinelli, and R. Simili, J. Phys.: Condens. Matter **14**, 3653 (2002).
[40]D. H. Auston, C. V. Shank, and P. LeFur, Phys. Rev. Lett. **35**, 1022 (1975).
[41]A. Vasil'ev, IEEE Trans. Nucl. Sci. **55**, 1054 (2008).
[42]T. R. Waite, Phys. Rev. **107**, 463 (1957).
[43]L. Rubin, O. Braginskaya, M. Isakova, N. Efremov, and V. Paschenko, J. Lumin. **29**, 399 (1984).
[44]C. F. Klingshirn, *Semiconductor Optics* (Springer-Verlag, New York, 1997).
[45]H. Nishimura, M. Sakata, T. Tsujimoto, and M. Nakayama, Phys. Rev. B **51**, 2167 (1995).
[46]F. Bertazzi, E. Bellotti, E. Furno, and M. Goano, J. Electron. Mater. **38**, 1677 (2009).
[47]K. Suzuki, S. Seto, T. Sawada, and K. Imai, IEEE Trans. Nucl. Sci. **49**, 1287 (2002).

[48]F. Antonangeli, N. Zema, M. Piacentini, and U. M. Grassano, Phys. Rev. B **37**, 9036 (1988).
[49]Y. Abraham, N. A. W. Holzwarth, and R. T. Williams, Phys. Rev. B **62**, 1733 (2000).
[50]V. N. Kolobanov, I. A. Kamenskikh, V. V. Mikhailin, I. N. Shpinkov, D. A. Spassky, B. I. Zadneprovsky, L. I. Potkin, and G. Zimmerer, Nucl. Instrum. Meth. A **486**, 496 (2002).
[51]V. Pankratov, A. I. Popov, I. Shirmane, A. Kotlov, G. A. Bizarri, A. Burger, P. Bhattacharya, E. Tupitsyn, E. Rowe, V. M. Buliga, and R. T. Williams (unpublished).
[52]V. Pustovarov, I. Ogorodnikov, A. Goloshumova, L. Isaenko, and A. Yelisseyev, Opt. Mater. **34**, 926 (2012).
[53]D. Fröhlich, B. Staginnus, and Y. Onodera, Phys. Status Solidi B **40**, 547 (1970).
[54]J. E. Eby, K. J. Teegarden, and D. B. Dutton, Phys. Rev. **116**, 1099 (1959).
[55]W. Martienssen, J. Phys. Chem. Solids **2**, 257 (1957).
[56]K. Teegarden and G. Baldini, Phys. Rev. **155**, 896 (1967).
[57]P. A. Rodnyi, *Physical Processes in Inorganic Scintillators* (CRC Press LLC, Boca Raton, FL, 1997), p. 79.
[58]A. Vasil'ev (private communication).
[59]V. Y. Timoshenko, A. B. Petrenko, M. N. Stolyarov, T. Dittrich, W. Fuessel, and J. Rappich, J. Appl. Phys. **85**, 4171 (1999).
[60]Y. Rosenwaks, B. R. Thacker, A. J. Nozik, Y. Shapira, and D. Huppert, J. Phys. Chem. **97**, 10421 (1993).
[61]R. Cohen, V. Lyahovitskaya, E. Poles, A. Liu, and Y. Rosenwaks, Appl. Phys. Lett. **73**, 1400 (1998).
[62]Y. Cui, M. Groza, D. Hillman, A. Burger, and R. B. James, J. Appl. Phys. **92**, 2556 (2002).
[63]U. Strauss, W. W. Rühle, and K. Köhler, Appl. Phys. Lett. **62**, 55 (1993).
[64]N. F. Massé, A. R. Adams, and S. J. Sweeney, Appl. Phys. Lett. **90**, 161113 (2007).
[65]Z. Wang, R. T. Williams, J. Q. Grim, F. Gao, and S. Kerisit, Phys. Status Solidi B (in press), doi: 10.1002/pssb.201248587.
[66]J. Q. Grim, K. B. Ucer, R. T. Williams, A. Burger, P. Bhattacharya, E. Tupitsyn, G. A. Bizarri, and W. W. Moses (unpublished).
[67]R. T. Williams, NNSA Workshop on Nonproportionality in Scintillators, Pacific Northwest National Laboratory, March 9, 2012 (unpublished).
[68]R. T. Williams, J. Q. Grim, and Q. Li, International Conference on Defects in Insulating Materials, ICDIM, 2012 (unpublished).
[69]F. Gao, Y. Xie, Z. Wang, S. N. Kerist, L. W. Campbell, R. M. V. Ginhoven, and M. P. Prange, International Conference on Defects in Insulating Materials, ICDIM 2012 (unpublished).
[70]A. Burger (unpublished).
[71]M. Couzi, J. Vignalou, and G. Boulon, Solid State Commun. **20**, 461 (1976).
[72]M. Fujita, M. Itoh, T. Katagiri, D. Iri, M. Kitaura, and V. B. Mikhailik, Phys. Rev. B **77**, 155118 (2008).
[73]J. Gabrusenoks, A. Veispals, A. von Czarnowski, and K.-H. Meiwes-Broer, Electrochim. Acta **46**, 2229 (2001).
[74]D. J. Singh, Appl. Phys. Lett. **92**, 201908 (2008).
[75]Y. Cui, R. Hawrami, E. Tupitysn, P. Bhattacharya, M. Groza, M. Bryant, V. Buliga, A. Burger, N. J. Cherepy, and S. Payne, Solid State Commun. **151**, 541 (2011).
[76]M. J. Weber and R. R. Monchamp, J. Appl. Phys. **44**, 5495 (1973).
[77]W. J. Van Sciver and L. Bogart, IRE Trans. Nucl. Sci. **5**, 90 (1958).
[78]Y. C. Shen, G. O. Mueller, S. Watanabe, N. F. Gardner, A. Munkholm, and M. R. Krames, Appl. Phys. Lett. **91**, 141101 (2007).
[79]M. Itoh, T. Katagiri, H. Mitani, M. Fujita, and Y. Usuki, Phys. Status Solidi B **245**, 2733 (2008).
[80]G. Hull, W.-S. Choong, W. Moses, G. Bizarri, J. Valentine, S. Payne, N. Cherepy, and B. Reutter, IEEE Trans. Nucl. Sci. **56**, 331 (2009).
[81]M. S. Alekhin, I. V. Khodyuk, J. T. M. de Haas, and P. Dorenbos, 11th Internnational Conference on Inorganic Scintillators and their Applications, Giessen, Germany, 2011 (unpublished).
[82]S. Kerisit, Z. Wang, R. T. Williams, J. Q. Grim, and F. Gao (unpublished).